J. Fluid Mech. (2004), *vol.* 516, *pp.* 265–301. © 2004 Cambridge University Press
DOI: 10.1017/S0022112004000709 Printed in the United Kingdom

Large-eddy simulation of a compressible flow in a three-dimensional open cavity at high Reynolds number

By LIONEL LARCHEVÊQUE[1]†, PIERRE SAGAUT[2,1], THIÊN-HIÊP LÊ[1] AND PIERRE COMTE[3,1]

[1]ONERA, CFD and Aeroacoustic department, F-92322 Châtillon, France

[2]Laboratoire de Modélisation en Mécanique, Université Paris VI, F-75005 Paris, France

[3]Institut de Mécanique des Fluides, 2 rue Boussingault, F-67000 Strasbourg, France

(Received 18 June 2003 and in revised form 17 March 2004)

Large-eddy simulations of a subsonic three-dimensional cavity flow with self-sustaining oscillations are carried out for a Reynolds number based on the length of the cavity equal to 7×10^6. Meticulous comparisons with available experimental data corresponding to the same configuration demonstrate a high level of accuracy. Special attention is paid to the mixing layer that develops over the cavity and two different zones are identified. The first one is dominated by Kelvin–Helmholtz instability, and the linear as well as quadratic energy transfers leading to the filling of velocity spectra are described. The Kelvin–Helmholtz instability also appears to be forced near the origin of the layer, and it is postulated that the small recirculation bubble located in this area is responsible for the forcing. Downstream of the first zone and up to the vicinity of the aft wall, the layer behaves very similarly to a free mixing layer by exhibiting a linear spreading. An influence of the recirculating flow inside the cavity upon the growth of the layer is nevertheless observed at downstream stations. Analysis of the pressure on the floor of the cavity reveals that the self-sustaining oscillation-related pressure modes (Rossiter modes) are independent of their spanwise location inside the cavity. On the contrary, Rossiter modes exhibit streamwise modulations and it is demonstrated that a very simple two-wave model is able to reproduce the spatial shape of the modes. Nonlinear interactions between Rossiter modes are encountered, as well as nonlinear interactions with low-frequency components. A joint time–frequency analysis shows a temporal modulation of the Rossiter mode levels at similar low frequencies, resulting in a special form of intermittency with competitive energy exchanges between modes.

1. Introduction

1.1. *Context of the study*

For both theoretical and practical reasons, flows past cavities have been intensively studied for decades since the pioneering works of Roshko (1955) and Karamcheti (1955), as illustrated in reviews by Rockwell & Naudascher (1978), Komerath, Ahuja & Chambers (1987) and Colonius (2001). Most of these studies, experimental,

---

† Present address: Aeronautics and Astronautic, School of Engineering Sciences, University of Southampton, Southampton SO17 1BJ, UK.

analytical and, more recently, numerical ones, focus on the strong self-sustained pressure oscillations that arise from the vorticity–pressure feedback loop encountered in this kind of flow. The few works including velocity data were either carried out for incompressible water flows (Gharib & Roshko 1987; Knisely & Rockwell 1982; Lin & Rockwell 2001) or low-Mach-number air flows (Sarohia 1975) with quite low Reynolds numbers. Cattafesta *et al.* (1997) performed 0.15 Mach number wind-tunnel tests with cavity length-based Reynolds numbers up to 1.6×10^6 and provide some shear-layer hot-wire measurements. On the other hand, technical advances render possible the experimental particle image velocimetry (PIV) (Forestier, Jacquin & Geffroy 2003) and numerical large-eddy simulation (LES) (Gloerfelt *et al.* 2002; Larchevêque *et al.* 2003) studies of cavity flows including velocity fields at high subsonic speed, but with a Reynolds number still remaining lower than one million. The goal of the present work is to provide an extensive description and analysis of both the pressure and of the velocity flow field for a subsonic flow past a cavity for a Reynolds number as high as 7×10^6. This is achieved by performing large-eddy simulations of a configuration for which only experimental pressure data are available.

1.2. *Physics of cavity flows*

Though some cavities known as closed cavities could lead to broadband noise when immersed into a flow field, the flow past cavities is generally characterized by large pressure oscillations at discrete frequencies, provided that the length of the cavity is long enough compared to the thickness of the incoming boundary layer (Sarohia 1975). These oscillations can originate from various phenomena which could involve fluid–structure interactions, but are mostly purely hydrodynamic in nature. We can briefly mention the ‘wake mode’ highlighted by Gharib & Roshko (1987) and in some recent numerical studies (Shieh & Morris 2001; Rowley, Colonius & Basu 2002; Gloerfelt, Bailly & Juvé 2003), where intense drag fluctuations are observed because of the ejection of very large vortices out of the cavity. Such behaviour seems to be preferentially related to two-dimensional or axisymmetrical configurations and, according to Rowley *et al.* (2002), could be partially due to an absolute instability.

Nevertheless, pressure oscillations are most frequently due to a coupling between the mixing layer developing over the cavity and the pressure field, and the resulting interaction is described as a ‘shear mode’ by Rowley *et al.* (2002). Following Rockwell & Naudascher (1978), this coupling can be classified as flow-resonant or flow-dynamic. For the first kind of interaction, the pressure part of the loop is due to the acoustic proper modes of the cavity. Plumbee, Gibson & Lassiter (1962) were the first to describe such mechanisms for a deep cavity, and East (1966) demonstrates that they generally occur for a low external velocity. Note that the inviscid theoretical proper modes’ frequencies of a cavity within the zero Mach number limit have been computed by Tam (1976).

For the flow-dynamic category, the pressure feedback is induced by the impact and stretching of the vortices of the shear layer at the aft edge of the cavity. The resulting pressure field outside the cavity is clearly deduced from the early schlieren visualizations by Karamcheti (1955), and a similar view issued from the present work is presented in figure 1. Comparisons with Karamcheti’s pictures reveal a more complex wave pattern outside the cavity in the present flow, presumably because of the much higher Reynolds number, thus leading to a highly turbulent region inside the cavity and in its vicinity. Karamcheti (1955) also highlights the influence of the nature of the incoming boundary layer on the levels of the fluctuations which are found to be higher for the laminar case.

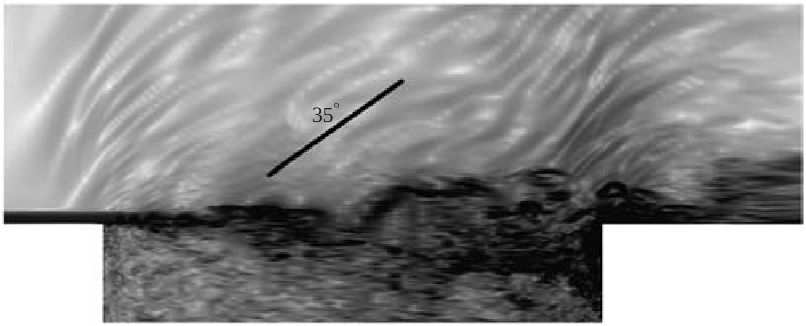

FIGURE 1. Instantaneous pseudoschlieren view issued from computation.

Another major contribution to the study of cavities belonging to the flow-dynamic category is the formula proposed by Rossiter (1964) to predict the frequency of the cavity tones. This formula is an adaptation of the one by Powell (1961) which predicts the resonant frequencies of the closely related problem of edge tones. The Rossiter formula reads:

$$f_n = \frac{U_\infty}{L} \frac{n - \gamma}{M_\infty + 1/\kappa}, \tag{1.1}$$

where U_∞ and M_∞ are the external flow velocity and Mach number, respectively, L is the length of the cavity, n is the mode number, and γ and κ are two constants adjusted from experiments. We generally consider $\kappa = 0.57$, γ being a function of the length-to-depth ratio L/D which varies from nearly zero for low ratio (deep cavity, see Larchevêque *et al.* 2003) to 0.57 for $L/D = 10$ (this latter bound is close to the upper ratio value leading to resonant cavity flows). Beside the prediction of the tone frequencies, the interest of Rossiter's works is to provide an a *posteriori* interpretation of (1.1) based on the identification of two phenomena which are responsible for the resonant loop: mixing-layer vortices moving downstream at velocity κU_∞ and pressure waves travelling upstream inside the cavity at the speed of sound. A vortex is created at the mouth of the cavity through the disturbances induced by upstream-travelling pressure waves and an upstream-travelling pressure wave is emitted at the downstream edge with a phase shift equal to γ after the impact of a vortex. Note that despite its rather simple construction, the semi-empirical formula (1.1) or its modified version for supersonic flow by Heller *et al.* (1973) have been used with great success to predict the frequencies of tones observed for a wide class of cavity flows. Note that because of this concordance, such tones will hereinafter be referred to as Rossiter modes.

Following Rossiter, by considering both a forced mixing layer and an acoustic feedback, multiple authors tried to reduce the empiricism of the approach by introducing in their models stability considerations for the shear layer. Some studies take into account infinitely thin vortex sheet stability (Bilanin & Covert 1973), with addition of image sources (Block 1976) to model reflections on the floor or including a pseudo-piston effect at the aft edge (Heller & Bliss 1975) so as to mimic the inflow/outflow process in this region, as highlighted by Spee (1966). Tam & Block (1978) introduced a finite layer thickness by means of hyperbolic tangent profiles similar to that used in the stability analysis by Michalke (1965) of a free mixing layer, and their results agree favourably with experiments.

Some experimental measurements related to incompressible or low-Mach-number flow (Sarohia 1975; Gharib & Roshko 1987; Cattafesta *et al.* 1997) confirm the similitude between free and cavity shear layers by demonstrating a linear growth for the layer at a rate that agrees with free shear-layer experiments. However, for high subsonic flow, studies by Gloerfelt *et al.* (2002), Forestier *et al.* (2003) and Larchevêque *et al.* (2003) suggest the existence of two linear regions, the first one located in the vicinity of the fore wall and leading to higher spreading rate. Forestier *et al.* (2003) pointed out that this characteristic resembles that observed for a subharmonic forced free shear layer known as 'collective interaction' (Ho & Huang 1982) which quickly yields large vortical structures from high-frequency small vortices. This explanation allows the authors to solve the paradox noted by Lin & Rockwell (2001) related to two different instabilities within the shear layer: Kelvin–Helmholtz related small-scale and large-scale structures such as those seen in figure 1 which are included in Rossiter's model.

Finally, even though the loop described by Rossiter predominates in flow-dynamics resonant cavity, secondary phenomena have been reported: pure acoustic modes (Heller, Holmes & Colvert 1971); three-dimensional effects (Maull & East 1963; Rockwell & Knisely 1980); nonlinear interactions with low frequency components (Knisely & Rockwell 1982) or between modes (Kegerise *et al.* 2004). The latter study also highlights a special form of intermittency for the Rossiter modes referred to as 'mode switching' by the authors, where the dominant Rossiter mode varies in time because of low-frequency amplitude modulations. The unsteady low-frequency variations of amplitude due to nonlinear interactions observed by Knisely & Rockwell (1982) may be related to this process.

1.3. *Description of the configuration*

The configuration used for this study is related to the extensive high-Reynolds subsonic cavity wind-tunnel tests carried out at QinetiQ, formerly Defence and Research Agency (DERA), UK. They made available a large amount of unsteady pressure measurements which are useful for computation validations (Henshaw 2000). The cavity is three-dimensional, with a length $L = 0.508\,\mathrm{m}$, the depth D and the width W being equal to 0.1016 m. The length-to-depth ratio $L/D = 5$ is such that the shear layer does not reattach on the floor of the cavity (open cavity), resulting in a cavity response of a flow-dynamic kind. The inflow Mach number $\mathrm{M} = 0.85$ was obtained from stagnation pressure $p_i = 99540\,\mathrm{Pa}$ and temperature $T_i = 301\,\mathrm{K}$, corresponding to a free-stream velocity of $U_\infty = 276.45\,\mathrm{m\,s^{-1}}$ and a cavity length based Reynolds number close to 7 million.

1.4. *Organization of the paper*

The paper is organized as follows. In § 2, the key elements of the numerical method used in this study are described briefly, including subgrid modelling, numerical schemes, time integration and boundary conditions. The validation procedure presented in § 3 is divided into two parts: a grid convergence study is described in § 3.1 while § 3.2 is devoted to spectral comparisons with the experimental pressure measurements.

The shear-layer mean properties such as the growth rate and spatial and temporal correlations are discussed in § 4, together with a description of the coherent structures dynamics. Spectral analysis of LES data is carried out in § 5: the mixing layer is studied in § 5.1, with emphasis on the initial region of the layer by means of cross and bispectral analyses; interpretations of pressure spectra on the floor of the cavity are provided in § 5.2, highlighting the presence of several different pressure modes; finally, joint time–frequency analyses are performed in § 5.3 so as to characterize the ‘mode switching’ phenomenon.

Lastly, the main results are summarized in § 6.

2. Numerical methods

Because of the high subsonic nature of the flow past the cavity, the compressible Navier–Stokes equations are considered. The LES equations are obtained using Favre filtering according to the formalism developed by Vreman, Geurts & Kuerten (1995), and the filtered equations are closed by means of a subgrid-scale viscosity and Prandtl analogy in a similar way to that proposed by Vreman *et al.* (1995). The whole process is further detailed in Larchevêque *et al.* (2003). The model retained to compute subgrid viscosity is the selective mixed-scale model introduced for compressible flows by Lenormand *et al.* (2000). This model relies on an estimation of the turbulent kinetic energy at the cutoff using a test filter coupled with a structural sensor based on the angle between vorticity and test-filtered vorticity.

Both spatial and temporal integration are carried out by means of second-order-accurate schemes. The spatial scheme belongs to the AUSM+(P) family and is described in Mary & Sagaut (2002). Time integration is performed through an implicit Gear like scheme (see Pechier, Guillen & Cayzac 2001, for details). Note that Raverdy *et al.* (2003) demonstrate the suitability of this approach for LES.

Because cavity flows exhibit strong pressure waves, it is of importance to ensure that the boundary conditions will not yield reflected waves that could affect the accuracy of the computation. In the present work, this is enforced by using non-reflective inflow/outflow characteristic-based treatment together with strong mesh stretching near the boundaries in the two directions related to the main propagation of the Rossiter pressure waves, namely the streamwise and vertical ones. The method was successfully used for the deep cavity flow LES by Larchevêque *et al.* (2003). The boundaries are also put far away enough from the cavity, with the distance on either side of the cavity zone equal to $1.55L \simeq 0.8\,\mathrm{m}$ for each of these two directions. Since no experimental data regarding the velocity field are available, the inflow velocity profiles are obtained from a thin boundary-layer simulation with a developing length set equal to the distance observed in the experimental set-up from the origin of the flat plate where the cavity model lies to the location corresponding to the inflow boundary. In the spanwise direction, symmetry conditions are set for boundaries located $0.7L \simeq 0.35\,\mathrm{m}$ away from the cavity.

Concerning the wall boundary conditions, two different treatments are used. The standard no-slip boundary condition is enforced for the five walls of the cavity. For the flat plate surrounding the cavity where the boundary layer can be approximated as a flat-plate boundary layer, a wall model based on a three-dimensional instantaneous viscous/logarithmic sublayer approach is used, with a typical first cell normal to the wall dimension of 70 wall units. Some details about this model can be found in Larchevêque *et al.* (2003).

3. Validation

3.1. *Grid convergence study*

Before validating the simulation by means of comparison with available experimental pressure data, we have to measure the influence of the mesh resolution and numerical

Computation	Mesh	Cells across initial vorticity thickness	Time step (s)	CFL max	Estimated cutoff frequency (Hz)
C	Coarse	8	10^{-5}	~ 20	$> 12\,500$
F	Fine	10	10^{-5}	~ 20	$> 12\,500$
C2	Coarse	8	2×10^{-5}	~ 40	> 6500

TABLE 1. Characteristics of the computations.

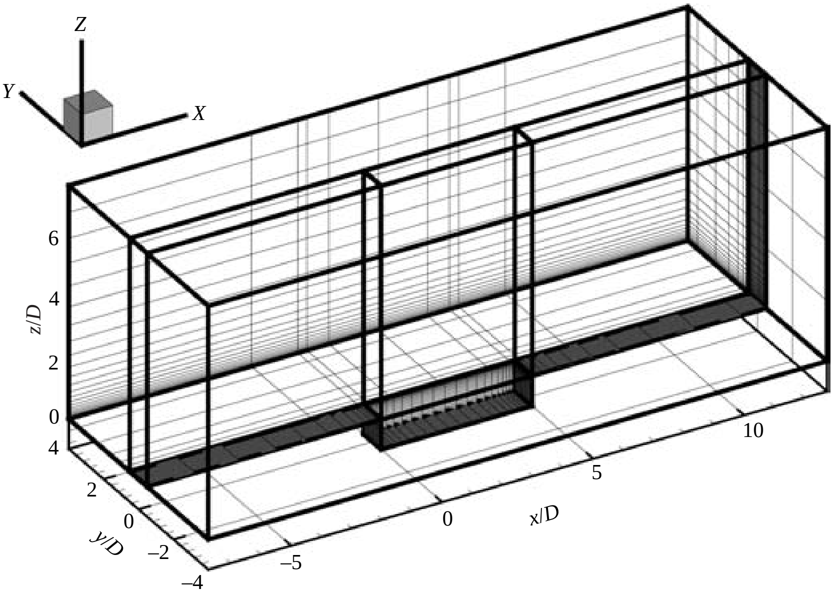

FIGURE 2. View of the coarse mesh: one every fourth cell is plotted.

scheme on the numerical results. Three different computations have been carried out in order to make sure that a grid-independent solution for the large structures is obtained. The main characteristics of the computations are detailed in table 1.

To evaluate the influence of grid resolution, two different multiblock meshes have been designed. The first one, referred to as the coarse grid, is plotted in figure 2. It includes about three million cells, with 100^3 of them inside the cavity, where the first layers are located 5×10^{-4} m away from the five walls. On the mixing layer horizontal centreplane, cells have a height of 3×10^{-4} m. In the streamwise x and vertical z directions, double hyperbolic tangent distributions are used, resulting in a stretch ratio of about 6%, while the mesh is uniform in the spanwise direction. The total number of cells has been significantly reduced by using local mesh refinement in the streamwise direction in subdomains located inside and over the cavity. See Mary & Sagaut (2002) for details of the specific treatment that is performed at the interfaces between blocks with different cell size. The second mesh has twice as many cells as the first one and is referenced as fine in table 1. The mesh refinement is obtained by multiplying the number of cells in both the transverse (y) and vertical (z) directions by 1.4 while keeping the cell sizes at domain boundaries unmodified. Simulations C and F use the coarse and fine grids, respectively. It is important that both grids have a sufficient number of cells across the boundary layer at the separation point, so that

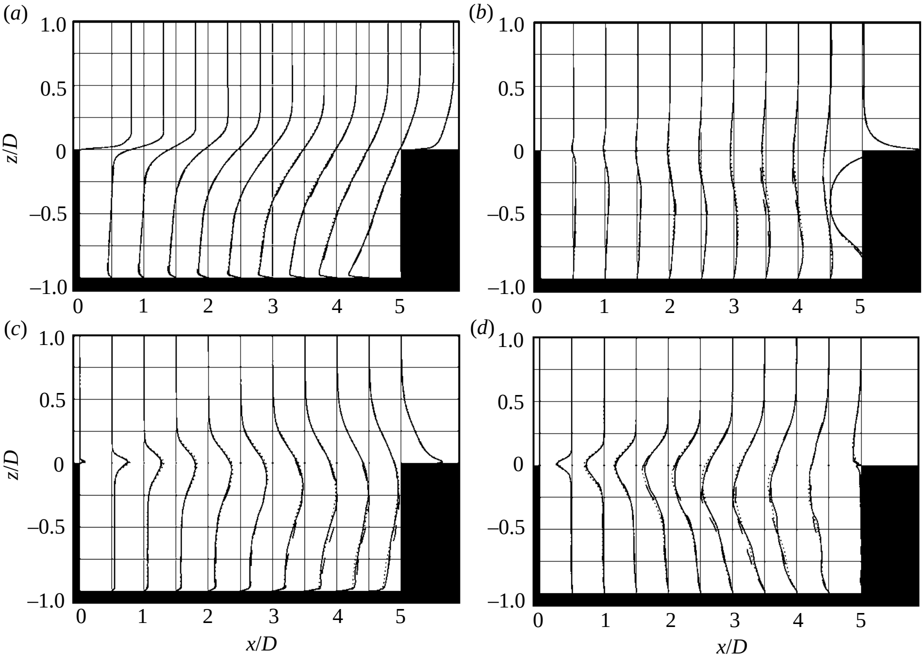

FIGURE 3. (*a*) Mean longitudinal velocity (*b*) mean vertical velocity (*c*) turbulent energy and (*d*) cross-Reynolds stress $u'w'$ profiles: ——, coarse mesh; · · ·, coarse mesh, $\Delta t \times 2$; — — —, fine mesh.

the initial growth of the separated shear layer over the cavity is correctly captured. Note that the grid resolution on the present coarse grid in that region of the flow is equivalent to that of the fine-grid simulation of the flow over a deep cavity presented in Larchevêque *et al.* (2003).

An additional computation, referred to as C2, is performed on the coarse mesh with a doubled time step in order to quantify the influence of the time step.

In this section, the comparison between simulations is related to the velocity field statistics only. The pressure spectra will be discussed in the next section, supported by the experimental data available. For all the computational cases, the statistical data have been collected over a physical sampling time of 0.5 s, after a relaxation time of 0.1 s from the beginning of the simulation which is necessary to obtain a statistically steady flow. The time of 0.5 s corresponds to more than 60 periods (based on the lowest Rossiter frequency) and therefore is long enough to obtain converged first- and second-order statistics.

The mean velocity profiles on the central (x, y)-plane are plotted in figure 3. The three computations obviously lead to very similar results. The main differences, which take place around $x/D = 3.5$ for the vertical velocity, w, are lower than 4% of the free-stream velocity and are related to very low velocities (one order of magnitude lower than the streamwise velocity levels, u, at the same place). Because the F computation departs from the very similar C and C2 simulations, the influence of the mesh resolution seems to prevail over the influence of the time step. The turbulent kinetic energy, k, and the shear stress profiles are presented in figure 3, leading to the same conclusion. The greatest difference is found once again at location $x/D = 3.5$, and is equal to about 10% of the local maximum value of k, showing that the coarse mesh is fine enough to resolve almost all the energetic eddies. However, because a

Peak number	1	2	3	4
Rossiter's formula†	148	357	566	775
Experiments	135	350	590	820
C computation	125	360	585	825
F computation	125	355	575	815
C2 computation	125	345	565	775

† Using $\kappa = 0.57$ and $\gamma(L/D \equiv 5) = 0.29$ as proposed in Larchevêque *et al.* (2003).

TABLE 2. Frequency (Hz) of pressure spectra peaks.

difference between coarse and fine mesh computations, although small, still exists, it is believed that a coarser grid should significantly alter the results. Despite the long sampling time used in this study, the shear stress does not seem to be fully converged in the lower downstream part of the cavity. At this location, the behaviour of the flow is highly unsteady because of the convection inside of the cavity of vortices strongly distorted by the downstream corner interaction. Moreover, such a process is able to create small structures with significant energy levels and thus it may explain the differences between the coarse and fine mesh simulations in this region.

As a conclusion, it is possible to state that grid convergence for the flow (in an LES sense) is reached.

3.2. *Comparisons with experiments*

As mentioned in § 1, the experimental cavity-flow database provided by QinetiQ (see Henshaw 2000) is used to validate the computation. The database includes instantaneous pressure measurements from multiple Kulite sensors located on the floor of the cavity, a quarter span from the sidewall. The sampling rate is 6 kHz, and the experimental sampling time is about 3.5 s, seven times larger than for the simulations. Because of the 'mode switching' phenomenon (Kegerise *et al.* 2004) that will be discussed in § 5.3, the experimental samples were split into seven blocks with equal lengths of 0.5 s. All the experimental results dealing with pressure fluctuations used in this section are therefore displayed as realizability intervals between the minimum and maximum values computed using these seven data blocks. The only exception is the frequency of the pressure peaks: because they exhibit very small variations in time, only the mean value over the seven block is considered. Notice that all the spectra have been computed using the parametric spectrum estimator of Burg (or maximum entropy method, see Childers (1978) for details and Huang & Ho (1990) for an example of use in the field of fluid mechanics). The ability of this method to generate spectrum estimators with accurately resolved peaks (for both the frequency resolution and the energy level) while smoothing the base noise level allows more flexibility than a classical fast Fourier transform periodogram in accurately comparing data with different sampling times and/or sampling rates. The method is also especially well-suited for short-time samples, a feature that will be used in § 5.3.

The frequencies of the main pressure modes are given in table 2. The unique value for each mode is due to the quasi-invariance of these values with regard to the location of the probes. The first line corresponds to the predictions issued from Rossiter's analytical model. It shows that, as expected, the peaks in the pressure spectra correspond to the Rossiter modes. Globally, the agreement between all the simulations and the experiments is very good. There is a small shift on the first mode.

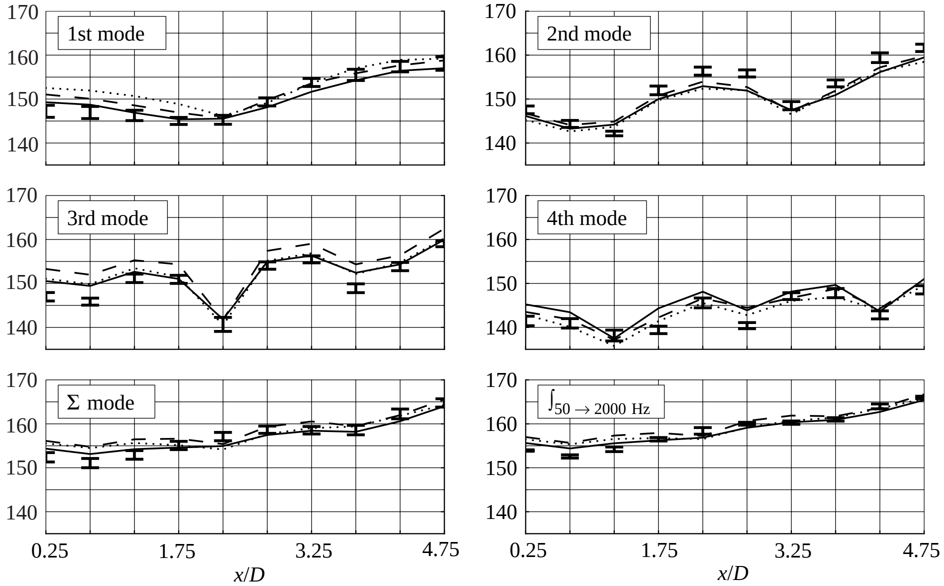

FIGURE 4. Streamwise evolution of band-integrated pressure fluctuation levels in BISPL (see table 3 for the band boundaries): ——, coarse mesh; · · ·, coarse mesh, $\Delta t \times 2$; — — —, fine mesh; =, experiments.

Rossiter mode	1	2	3	4
Lower bound (Hz)	75	300	550	750
Upper bound (Hz)	175	400	650	850

TABLE 3. Bounds for integration of the pressure spectra.

The C2 computation exhibits a more significant discrepancy for the higher mode that could be attributed to larger numerical errors.

To obtain a global representation of the Rossiter peak energy levels for each simulation at multiple locations, the pressure spectra have been integrated over frequency bands which encompass each peak frequency, with the streamwise evolution of the resulting energy levels plotted in figure 4. All frequency bands have a width equal to 100 Hz and are centred on the mean Rossiter mode frequencies, as shown in figure 5 which will be further analysed. The detailed frequency band boundaries can also be found in table 3. Because of their small width and because the peak levels are 10 dB greater than the base noise level, the values computed using this procedure are fully significant. In addition to each single Rossiter mode energy level, the sum over all the Rossiter modes and the total energy inside the band (50 Hz–2000 Hz) are also displayed. Note that for this last plot, the upper boundary has been reduced from the theoretical maximum of 3 kHz to 2 kHz to prevent any misinterpretation due to the use of a filter during the post-processing of wind-tunnel data in order to alleviate aliasing problems. Globally, the three simulations yield the same error level on Rossiter modes, lower than 5 dB for all modes at all locations. Such error levels are far better than those commonly observed in unsteady RANS studies (see Grace 2001, for some examples). Moreover, the spatial mode shapes are predicted

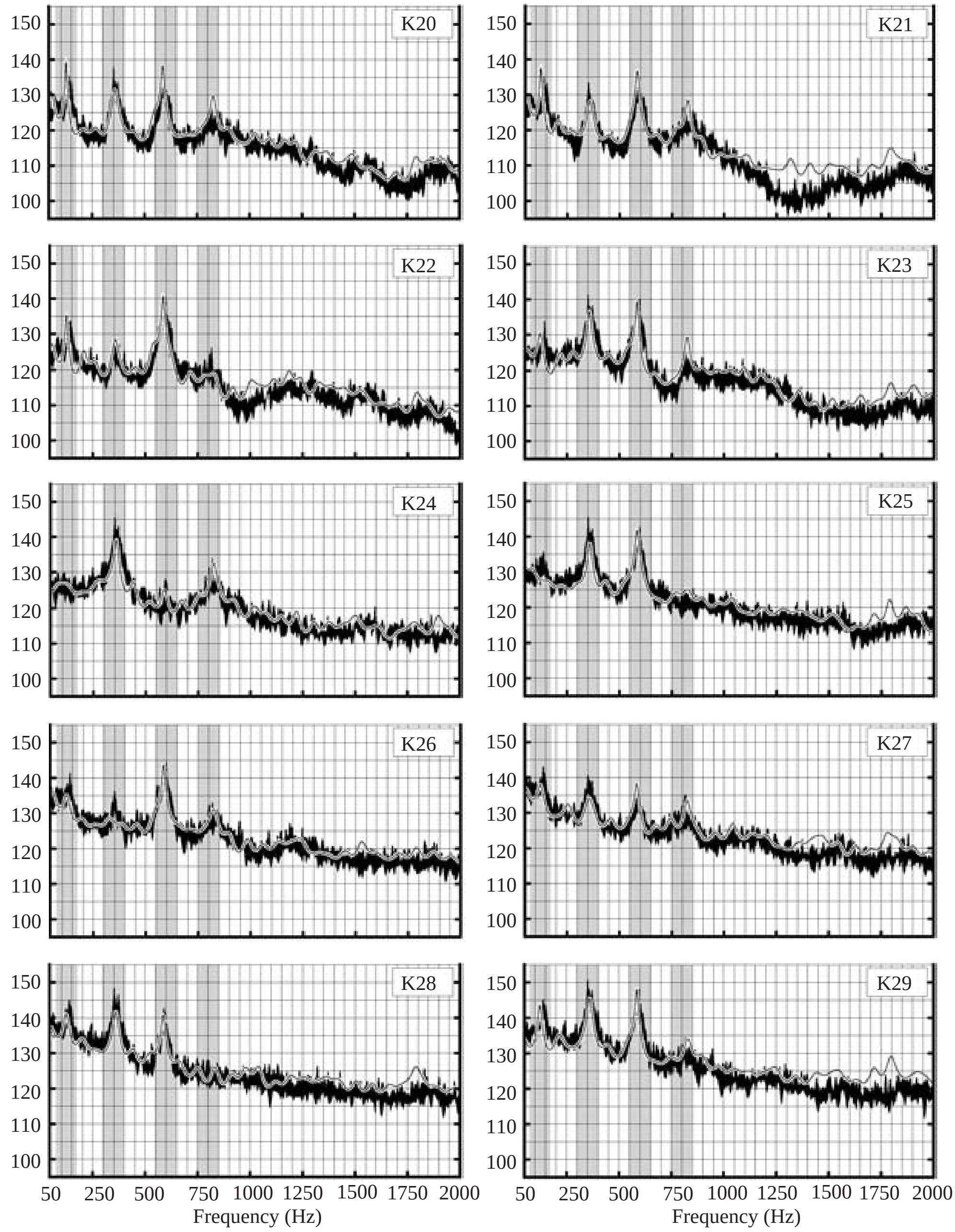

FIGURE 5. SPL pressure power spectra from experiments (black areas) and C computation (black line surrounded with white) for the ten microphones located on the floor of the cavity. Grey bands correspond to frequencies over which spectra have been integrated to obtain the results presented in figure 4.

well. Because the second mode tends to be under-predicted while the third one is generally over-predicted, the error level related to the total energy over all modes is reduced, demonstrating that even if there are some small discrepancies regarding the distribution of energy among modes, the pressure fluctuation energy related to the

Rossiter phenomenon is very accurately computed. The 'total' pressure energy levels show a similar predictive quality. For the 'total' energy, the uncertainty gap related to the 'mode switching' phenomenon is greatly reduced when compared to the total energy contained in Rossiter modes despite very similar energy levels. This highlights some form of pressure energy redistribution in time between the base noise and peak parts of the spectra.

Some of the advanced spectral analyses that will be presented in § 5 are based on the storage of the full instantaneous field at each time step and therefore require a very large amount of disk storage. As C and F simulations are in equally good agreement with the experimental measurements, the C computation has been retained in order to minimize disk storage and computational time requirements. The C2 computation, which could have reduced these requirements even more, has been rejected because of the small discrepancy on the prediction of fourth mode frequency. Consequently, the remaining part of this paper is related to data coming from the C computation only. Therefore, in order to ensure a high level of confidence for the forthcoming analysis, the evaluation of the C simulation has to be studied thoroughly.

Figure 5 shows pressure spectra for the ten Kulite sensors. The capability of the simulation for an accurate prediction of the pressure peak levels observed in figure 4 is confirmed. The errors on the second mode at locations $1.75 \leqslant x/D \leqslant 2.75$ that were present in figure 4 are lowered because they arise from a small difference in the peak width rather than a difference in peak levels. To summarize the small discrepancies between the computation and the measurements, we note a slight under-prediction of the frequency of the first mode, some peak level under- and over-predictions for modes 2 and 3, respectively, and a coherency which is too high for the fourth mode. Nevertheless, the description of the Rossiter related phenomena can be held as very accurate. The base levels are also in very good agreement with the experiments, with the correct spatial dynamics over the whole cavity length. Two discrepancies are nonetheless discernible: a local one at $x/D = 0.75$ around 1300 Hz with a rather large over-prediction of the base noise level and a more global one, which tends to sharpen the smooth bump around 1900 Hz observed in wind-tunnel experiments.

Both spatial and spectral accuracy of the computation having been validated, cross-spectra can be used to check the ability of the computation to recover information dealing with phases and therefore indirectly to evaluate the accuracy of the recovery of the propagation process on the floor of the cavity. The cross-spectrum estimator reads:

$$S_{XY}(f) = \langle \hat{X}(f)\hat{Y}^*(f) \rangle, \tag{3.1}$$

where $\hat{\chi}(f)$ is the windowed fast Fourier transform of the time series $\chi(t)$, the asterisk indicates complex conjugation and $\langle . \rangle$ is an averaging operator. A convenient way to analyse the complex cross-spectrum is to decompose it into two spectra, the squared coherence spectrum and the phase spectrum, respectively, defined by:

$$Co^2_{XY}(f) = \frac{|S_{XY}(f)|^2}{S_{XX}(f)\, S_{YY}(f)}, \qquad Ph_{XY}(f) = \tan^{-1}\left\{ \frac{\mathrm{Im}\,[S_{XY}(f)]}{\mathrm{Re}\,[S_{XY}(f)]} \right\}. \tag{3.2}$$

In order to obtain reliable results, $\langle . \rangle$ has to be performed over a sufficient number of blocks. In the present study, 50 windowed blocks with 50% overlapping are used. This process is applied to both experimental and computational data, thus resulting in smooth estimators, but with a poor frequency resolution of nearly 50 Hz. The corresponding graphs are presented for short (1.5 D, figure 6*a–c*) and large (4.5 D,

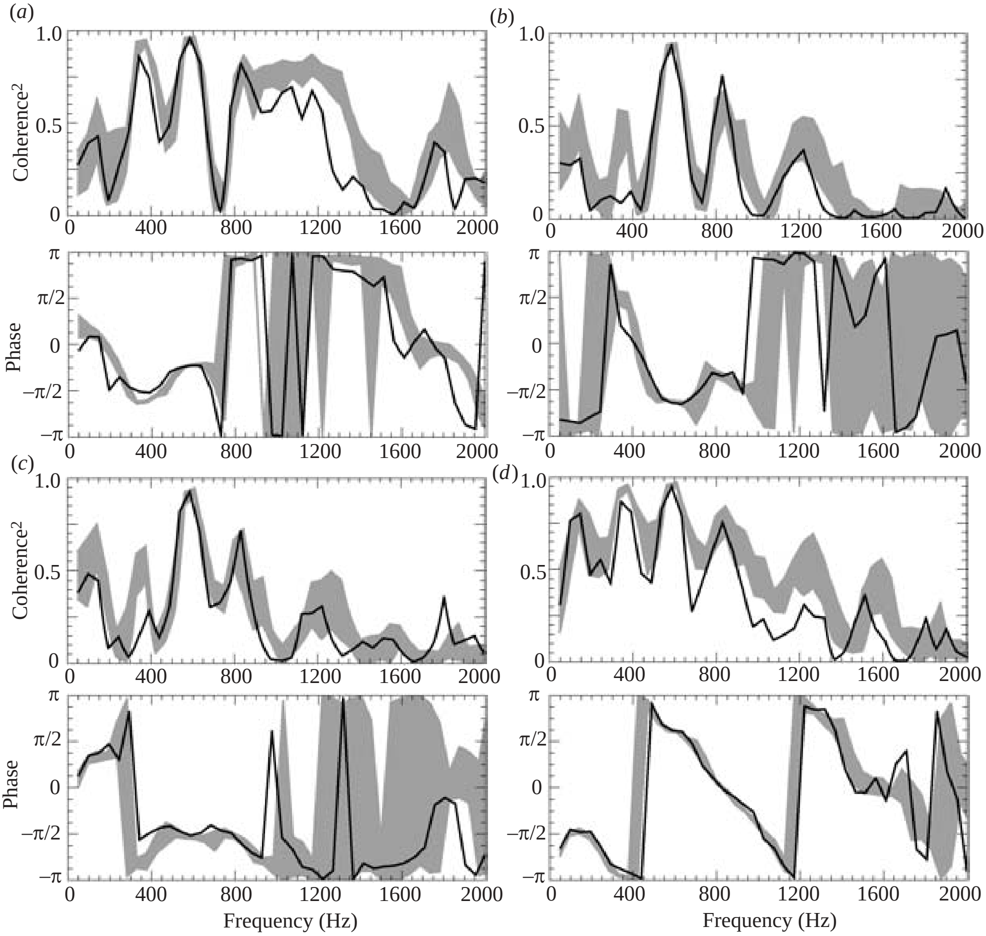

FIGURE 6. Coherency and phase pressure spectra between locations (*a*) $x/D = 0.25$ and $x/D = 1.75$, (*b*) $x/D = 1.75$ and $x/D = 3.25$, (*c*) $x/D = 3.25$ and $x/D = 4.75$ and (*d*) $x/D = 0.25$ and $x/D = 4.75$: experiment (grey area) and C computation (black line).

figure 6*d*) streamwise separation lengths, respectively. Considering the squared coherence spectra, the agreement is good even for the higher frequencies at large distance. The only exception is for the second Rossiter peak between locations $x/D = 1.75$ and $x/D = 3.25$, $x/D = 3.25$ and $x/D = 4.75$. This is probably due to a more evanescent mode at station $x/D = 3.25$ in the computation than in the experiments (see figure 5). The phase spectra issued from the computation are in excellent agreement with the experimental ones despite the slight difference in the spectral resolution which induces small frequency shifts; other discrepancies occur in frequency bands where the squared coherence is low, and therefore are not significant.

A very complete spectral analysis has revealed that all the simulations, and more precisely the C simulation, exhibit most of the observable features of the experiments. Note particularly that the Rossiter modes are predicted very well in frequencies (that is rather common) and in levels (that is far more unusual) over the full cavity length. The capability of LES to predict shallow-cavity flow has therefore been demonstrated. The remaining part of this paper will illustrate its capability to improve the understanding of this class of flow using the instantaneous three-dimensional data fields.

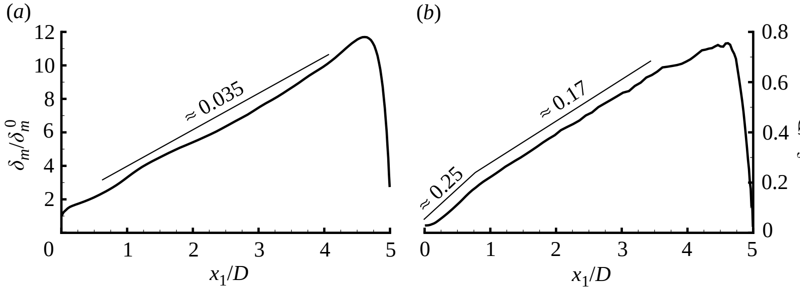

FIGURE 7. (*a*) Momentum thickness and (*b*) vorticity thickness evolution along the mixing layer.

4. Mixing layer mean flow analysis

A first analysis of the mixing layer is carried out by computing its momentum and vorticity thicknesses. Because of the existence of a strong recirculating region (see figure 3), the correct definitions of these thicknesses are non-trivial because they rely on the choice of a characteristic velocity inside the cavity. The few cavity studies there are which include data on shear-layer thickness generally neglect the influence of the reverse flow. The same approach is retained for the present study. Nevertheless, thicknesses based on the local true value of the larger reverse velocity have also been computed, and differences resulting from the use of these definitions will be highlighted when encountered. Also note that even though high subsonic flow is considered, the incompressible definition for momentum thickness is retained so as to allow direct comparison with the aforementioned cavity study. We have nonetheless to specify that compressible momentum thickness has been computed too and results in only minor alteration of the results detailed hereinafter. Such a low influence of the compressibility effects makes sense because the convective Mach number is overall lower than 0.55. The momentum thickness definition eventually reads:

$$\delta_m(x,y)=\int_{z_0(x,y)}^{+\infty}\frac{u(x,y,z)}{U_\infty}\left[1-\frac{u(x,y,z)}{U_\infty}\right]\mathrm{d}z,\qquad z_0(x,y)=\max\{\zeta/u(x,y,\zeta)\equiv 0\}. \tag{4.1}$$

The resulting plot for the plane $y/D=0$ is drawn in figure 7(*a*). Note that all the planes $z/D\in[-0.25, 0.25]$ lead to two series of almost superimposed lines. The layer is found to have a growth rate within the range [0.03, 0.04] for most of the length of the cavity. Multiple turbulent free mixing-layer experiments lead to similar results, even if the layer is forced (Huang & Ho 1990). Focusing now on mixing layers over cavities, and restricting ourselves to the case of a turbulent incoming boundary layer, spreading rate values very close to the present one have also been observed for various length to depth ratios at similar Mach numbers (see table 4). However, the previous observations listed in this table show the existence of an initial high spreading rate region. It has been postulated, for instance in Forestier *et al.* (2003), that this characteristic was due to an early pairing of the coherent structures ('collective interaction' as referred to by Ho & Huang 1982) triggered by a strong forcing associated to pressure waves. The absence of such an initial region in the present case could therefore be explained as a consequence of the large streamwise extent of the cavity (more than ten times larger than cavities considered in the references given in table 4). The upstream travelling pressure waves related to the Rossiter feedback

Reference	Nature	M	L/D	L/δ_m^0	Re_L	$\partial\delta_m/\partial x$
Forestier *et al.* (2003)	Exp.	0.8	0.41	77	8.6×10^5	0.04
Larchevêque *et al.* (2003)	LES					
Gloerfelt *et al.* (2002)	LES	0.8	3	65	1.5×10^5	0.03
Present study	LES	0.85	5	328	7×10^6	0.03–0.04

Table 4. Comparison of growth rate of mixing-layer momentum thickness for cavities with turbulent incoming boundary layer.

mechanism may then suffer a higher total damping and scrambling through wave dispersion all along the highly inhomogeneous mixing layer, resulting in a weaker and less coherent forcing unable to really accelerate the pairing of the structures. Another possible influence is the unsteady three-dimensional flow at the upstream corner that affects the very beginning of the mixing layer where the ‘collective interaction’ is supposed to take place. These hypotheses are nonetheless difficult to check as the ‘collective interaction’ itself is difficult to characterize in cavity flows.

Though generally less studied because of the difficulty in obtaining reliable experimental data dealing with velocity gradients, the vorticity thickness is also of interest. It is defined as:

$$\delta_\omega(x, y) = \frac{U_\infty}{\max_{[z]}\left[\dfrac{\partial u(x, y, z)}{\partial z}\right]}. \tag{4.2}$$

From figure 7(*b*), it is observed that the mixing layer is roughly composed of two regions before its inner structure is annihilated in the vicinity of the aft corner. The first region is located between $x/D = 0.1$ and $x/D = 0.7$ ($6 \leqslant x/\delta_m^0 \leqslant 45$). Within these bounds, the mixing layer exhibits a large growth rate of 0.25. The other region is characterized by a lower linear growth rate of 0.17. In this second zone, the extension of the linear region is wider when the reverse velocity inside the cavity is taken into account to compute δ_ω. This illustrates the fact that in the downstream part of the cavity the recirculating flow is strong enough to influence the local state of the layer whose thickness is of the same order of magnitude as the depth of the cavity. Finally, note that in this second region, the ratio between the spreading rates of momentum thickness and vorticity thickness reaches a value close to 1/5 which is commonly observed for a fully developed free mixing layer (see Browand & Trout 1985).

Concerning the high initial spreading rate, it seems reasonable to postulate that it is due to the existence of nearly two-dimensional tubes of vorticity originating from the Kelvin–Helmholtz (K–H) instability. For instance, in Larchevêque *et al.* (2003), an initial high growth rate up to $x/\delta_m^0 \leqslant 40$ was well correlated with two-dimensional vortices. The rate was in fact 2.5 times higher than the present one, but this difference can be seen as another clue to the lower coherent forcing already mentioned.

Some evidence of the presence of two-dimensional structures can be obtained by computing two-point spatial transverse correlations in the region defined above. Figure 8 presents the normalized correlations with regard to the transverse distance ξ for u in the part $\xi > 0$ and w in the part $\xi < 0$. For both velocity components, the spanwise correlation length obviously decreases as the distance to the leading edge of the cavity increases and tends to reach a plateau beyond $x/D \simeq 0.7$. Such behaviour is expected for a mixing layer up to its transitional state. We have to specify that downstream this location and up to the aft wall influence region, the correlation length

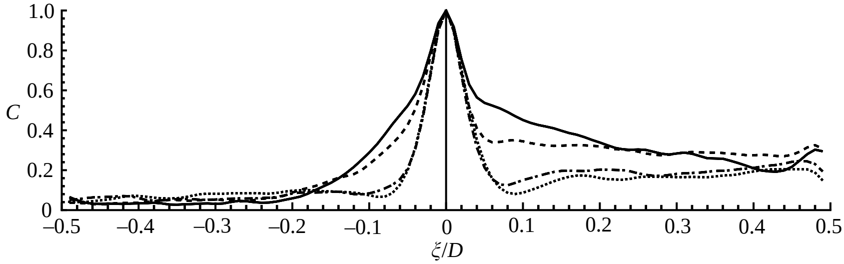

FIGURE 8. Spanwise two-point auto-correlation of u ($\xi/D \geqslant 0$) and w ($\xi/D \leqslant 0$) at locations: ——, $x/D=0.1$; – – –, $x/D=0.3$; –·–, $x/D=0.5$ · · ·, $x/D=0.7$.

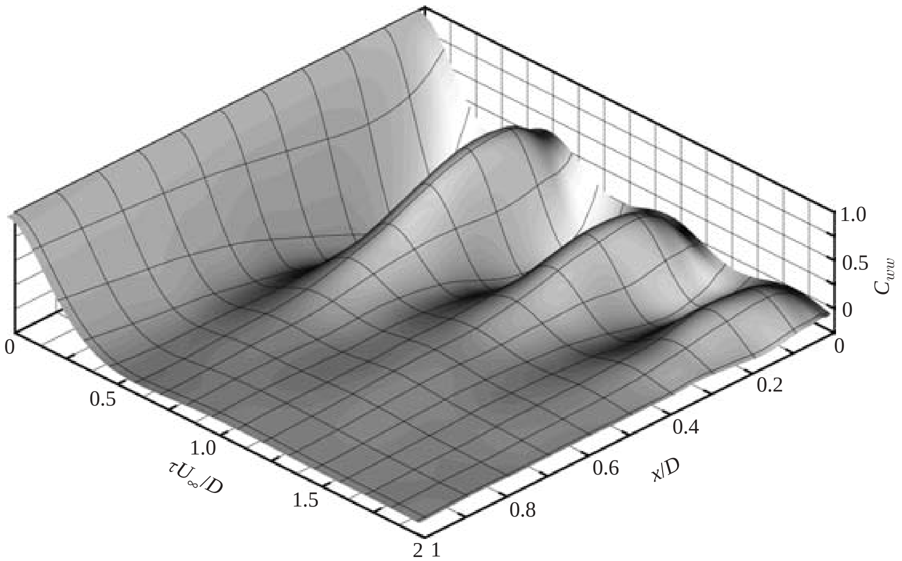

FIGURE 9. Evolution of temporal normalized auto-correlation $C_{ww}(\xi=0,\tau)$ for vertical velocity w along the line ($y/D=0, z/D=0$).

rises again, as observed in the free shear layers by Browand & Trout (1985) after mixing transition. The non-vanishing correlation for large distances observed for the streamwise velocity component is a consequence of the crossing of upstream travelling two-dimensional strong pressure waves. Because of this propagation direction, w is less altered and exhibits a standard zero correlation for large ξ.

In order to characterize the K–H instability, its fundamental frequency has to be estimated. Following Browand & Trout (1985), this can be done by looking at the mean vortex-passage period T_p defined as the time interval to the first peak of the velocity fluctuation auto-correlation function. Based on figure 8, the vertical velocity w is retained in order to alleviate misinterpretation due to the crossing of the Rossiter pressure waves. The temporal normalized auto-correlation as a function of x/D is presented in figure 9, and significant temporal correlation levels are observed in the above-mentioned region $x/D \leqslant 0.6$. At the maximum correlation location $x/D=0.15$, T_p is found to be equal to $0.61\,D/U_\infty$, corresponding to a frequency of 4460 Hz. Using the local vorticity thickness and $\overline{U}=U_\infty/2$, the normalized frequency is found to be equal to $St=0.14$. This value compares very well with $St=0.135$ found by means of linear stability analysis performed by Monkewitz & Huerre (1982). Adding

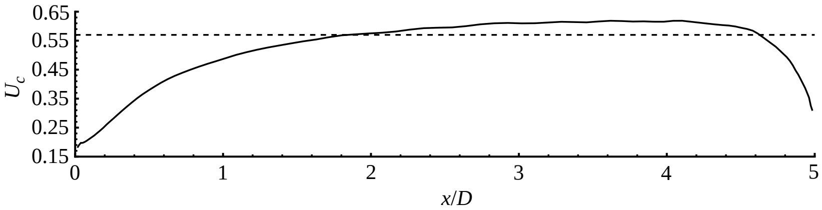

FIGURE 10. Convection velocity estimated using two-point two-time auto-correlation of vertical velocity: ——, numerical results; — — —, $U_c = 0.57$.

this information to the previous elements, we are finally able to conclude that the K–H instability is dominant in the initial region of the mixing layer and therefore should be partially correlated to the large spreading rate observed at these locations. However, note that beyond $x/D = 0.15$, the faster increase for δ_ω than for T_p results in rapidly growing values for the Strouhal number. This has already been mentioned by Browand & Trout (1985) for free mixing layers, but the final value of $St = 0.39$ at $x/D = 0.6$ is 35% larger than the largest values observed by these authors. This implies the existence of a mechanism complementary to the basic K–H instability so as to explain the higher growth rate in the vicinity of the fore wall. Note that instantaneous vortical structure visualizations do not seem to exhibit pairing, making it difficult to invoke the 'collective interaction' to identify this auxiliary mechanism. The spectral analysis of the mixing layer that will be presented in § 5.1 will provide more information regarding this point.

A last item of information related to the mixing layer is the convection velocity of the coherent structures. To obtain this, a classical procedure based on the two-point two-time correlations along the line $(y/D = 0, z/D = 0)$ is used. The variable retained for the correlation is the vertical velocity component because it is less sensitive to the pressure waves than u as already seen in figure 8. The evolution of the convective velocity is drawn in figure 10. In addition, a dashed line is plotted which corresponds to the convective velocity that was retained when estimating Rossiter mode frequencies. Roughly, two regions are discernible. The first one exhibits a constant acceleration and extends nearly over the region where two-dimensional structures have been highlighted. It is worth noting that a similar link between strong two-dimensionality and constant acceleration of the structures has already been observed in the cavity studied by Larchevêque *et al.* (2003). The second region is located within the range $2.8 \leqslant x/D \leqslant 4.4$ $(180 \leqslant x/\delta_m^0 \leqslant 285)$: after a relaxation zone, the velocity tends toward a plateau corresponding to the value $169\,\mathrm{m\,s^{-1}} = 0.61\,U_\infty$, close to that of $0.6\,U_\infty$ observed by Ahuja & Mendoza (1995) for small structures in a weakly compressible cavity. Finally, because of the influence of the aft wall, the velocity drops very fast. The mean value of the convective velocity over the whole mixing layer is equal to $0.53\,U_\infty$, quite comparable with the Rossiter classical value of $U_c = 0.57\,U_\infty$ because of the uncertainty of the estimator.

5. Spectral analysis

5.1. *Velocity and pressure inside the mixing layer*

5.1.1. *Global analysis*

The spectral analysis presented in this section deals with the use of data extracted from the plane $z = 0$. Because the maximum value of the vertical velocity gradient

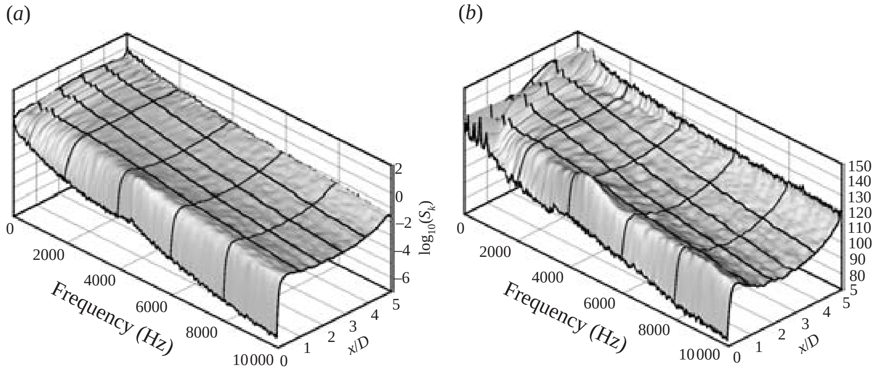

FIGURE 11. Spectral surfaces along the longitudinal centreline of the mixing layer $(y/D=0, z/D=0)$: (*a*) turbulent kinetic energy and (*b*) pressure fluctuations.

is located in the very vicinity of this plane in almost all the open surfaces of the cavity, this geometric boundary is fully representative of the true mixing-layer centre. The storage of instantaneous velocity and pressure data over the whole plane therefore allows the local spectral characteristics of the mixing layer to be studied. The spectra have been computed using FFT averaged over 24 blocks with a 50% overlap resulting in a 24 Hz spectral resolution. For the sake of clarity, the spectra have also been slightly smoothed to remove the residual noise. We checked that this procedure did not alter the levels of the peaks.

A first example of this approach is found in figure 11 which presents the evolution of the turbulent kinetic energy (TKE) $k=0.5(u'^2+v'^2+w'^2)$ (figure 11*a*) and pressure spectra (figure 11*b*) along the line $(y=0, z=0)$. Both spectra can be roughly decomposed into three regions with respect to the x-axis. The first one, which corresponds to the zone where the K–H instability has been identified in § 4, is characterized by a rapid increase of the global energy level. A bump centred on the frequency related to this instability mechanism is also clearly seen, and the energy contained in that bump is larger than the one related to Rossiter modes. Note that this region will be dealt with separately in § 5.1.2. The second region is located between $x/D=1$ and $x/D=4$, where there is very little evolution in the global shapes and levels of the spectra. In the vicinity of the aft wall, the large layer flapping due to the inflow/outflow process (Rockwell & Knisely 1979) yields an increase of the fluctuating kinetic energy. Focusing on the Rossiter frequency band, it is obvious that the Rossiter modes are mainly pressure modes and do not have a large impact on the velocity field. We can also remark on the streamwise modulation of the mode peak levels in the pressure spectrum.

Spectra are also modulated with regard to the transverse position, as can be seen in figures 12 and 13, which display the TKE and pressure spectra at four equidistant locations in the streamwise direction, respectively. For the first one, namely $x/D=0.25$, both TKE and pressure exhibit the above-mentioned bump with very similar shapes. More precisely, we observe an almost constant level in the half transverse central part of the cavity, and a noticeable decrease near the transverse walls. This feature agrees well with the existence of a confined K–H instability. The fact that the pressure spectra also exhibit such damping near the walls illustrates that the phenomenon has a hydrodynamic rather than an acoustic origin. At the three other locations, the bump is no longer observed and the spectrum is characterized by

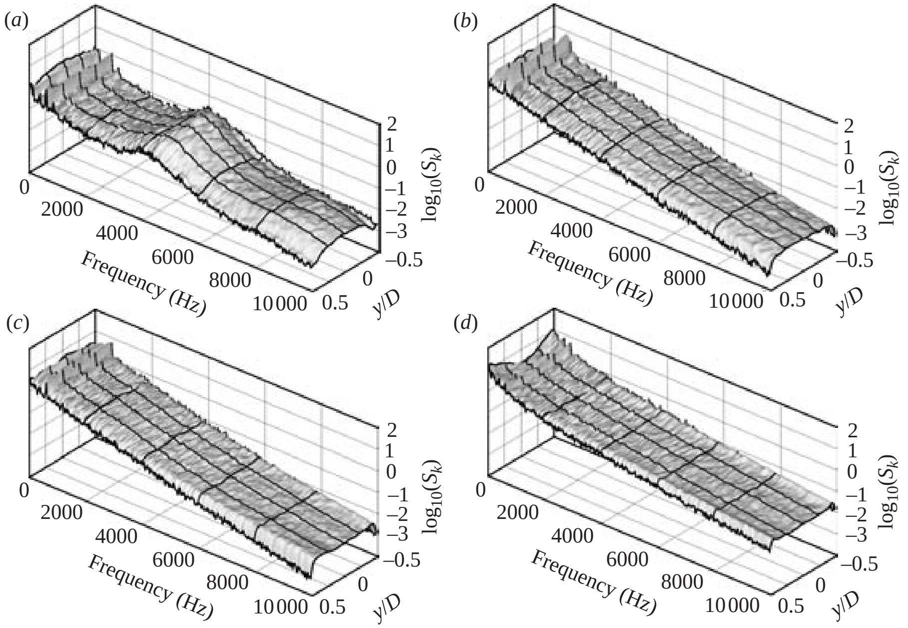

FIGURE 12. Spectral surfaces of turbulent kinetic energy in the mixing layer at four different locations on the x-axis corresponding to locations (a) $x/D = 0.25$, (b) $x/D = 1.75$, (c) $x/D = 3.25$ and (d) $x/D = 4.75$.

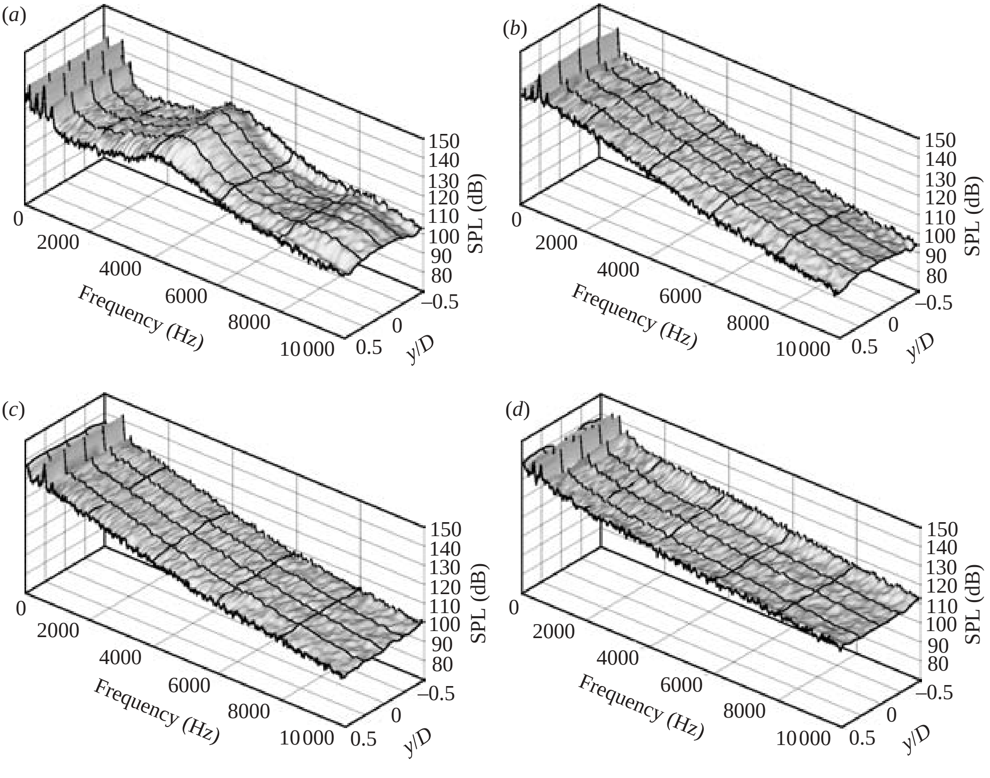

FIGURE 13. Spectral surfaces of pressure fluctuation in the mixing layer at four different locations on the x-axis corresponding to locations (a) $x/D = 0.25$, (b) $x/D = 1.75$, (c) $x/D = 3.25$ and (d) $x/D = 4.75$.

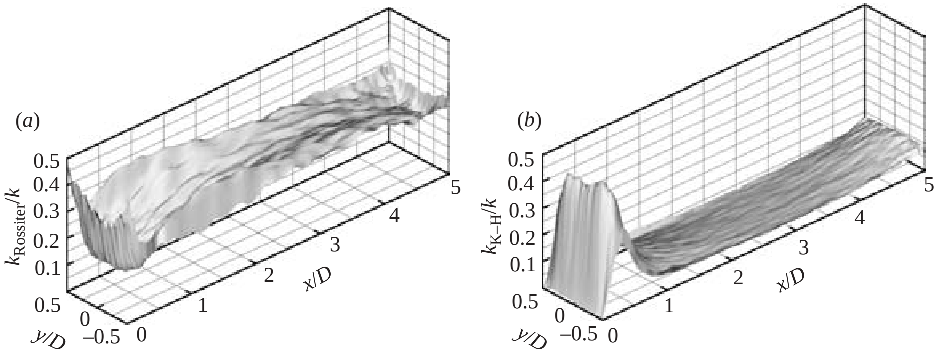

FIGURE 14. Band integrated turbulent kinetic energy inside the shear layer normalized using the local total turbulent kinetic energy: sum of (*a*) Rossiter modes and (*b*) K–H instability.

a smooth slope beyond 1000 Hz, the TKE spectrum being only slightly affected by transverse walls. Note that at the last station, the TKE spectrum exhibits an inertial range with a $-5/3$ slope for about half a decade.

Concerning the low-frequency region, the Rossiter mode peaks are not only less prominent in the TKE spectra with respect to pressure spectra, but they are also less two-dimensional. Nevertheless, the transverse modulation, even for the Rossiter modes, is low enough to allow us to conclude that the flow can be considered as being homogeneous in the spanwise direction within the bounds $y/D \in [-0.25, 0.25]$ over most of the x-axis. The main exception takes place near the aft wall where the strong streamwise vortices ejected near the corners induce a strong low-frequency three-dimensionality that can be clearly seen in figure 12(*d*).

Since the frequency band related to the K–H instability has been clearly identified, it is possible to characterize the corresponding energy by integrating the spectrum. Therefore, the region [3000 Hz, 6000 Hz] comes in addition to the bounds presented in table 3. This allows us to analyse the relative local dominance of the two processes that have been highlighted in the mixing layer. The spatial evolution of the energy contained inside the K–H band and in the four Rossiter modes is presented in figure 14, normalized by the total variance of the signal. It is obvious that in the region where the K–H instability occurs, the associated velocity fluctuations are larger than that induced by the Rossiter modes. Nonetheless, we can see that in the vicinity of the fore wall, where velocity is low, the contribution of the Rossiter modes is significant. Beyond $x/D = 0.7$, there is no process other than the turbulent cascade to supply the former K–H frequency band with energy, resulting in a rapid drop of the kinetic energy in this frequency band. On the contrary, the Rossiter modes account for up to 40% of the total velocity fluctuations near $x/D = 1$. The relative levels then slowly decrease because of the fill up of the higher frequencies through the turbulent energy cascade, but Rossiter modes still remain responsible for about a third of the fluctuations. However, note that such results have to be moderated slightly since velocity Rossiter peaks do not usually emerge from the background level. Therefore, the energy contained in frequency bands related to Rossiter modes could be affected by other hydrodynamic low-frequency phenomena.

The pressure spectra do not suffer from such restrictions and the analysis of the Rossiter mode contribution to the total energy is presented in figure 15(*a*). It can be seen that apart from the K–H region, Rossiter modes are responsible for roughly half of the fluctuating energy. In the initial region where the turbulence level is lower, the

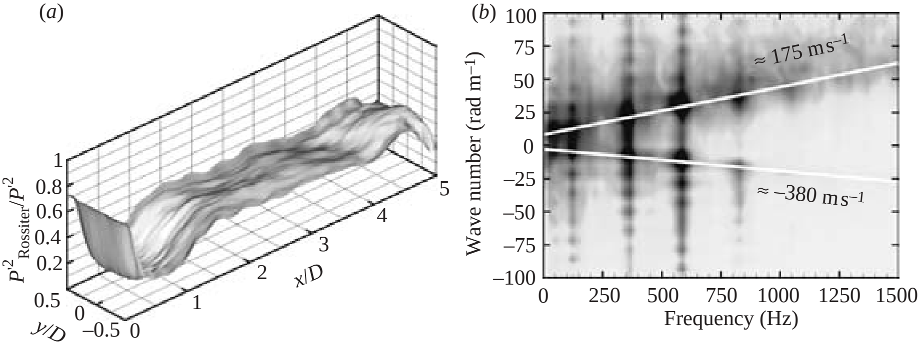

FIGURE 15. Characteristics of the Rossiter modes inside the mixing layer: (*a*) pressure fluctuations related to Rossiter mode frequency band normalized using the local total pressure fluctuation value and (*b*) frequency–wavenumber pressure spectrum along the line ($y/D=0$, $z/D=0$).

value can even grow up to 75%. The amplitude of Rossiter modes inside the mixing layer being known, we can also evaluate their phase velocity. To compute it, we may use a frequency–wavenumber spectrum along the line ($y/D=0, z/D=0$) since it has been shown that pressure Rossiter modes are almost insensitive to spanwise location. The spectrum estimator Φ, based on the cross-spectrum between points x_i and x_j, reads:

$$\Phi(f,k)=\exp(\sqrt{-1}\,k\,x_i)S_{x_i\,x_j}(f)\exp-(\sqrt{-1}\,k\,x_j). \tag{5.1}$$

The result is displayed in figure 15(*b*). Two mean propagation speeds are identified: one forward at a normalized velocity of nearly $175\,\mathrm{m\,s^{-1}}=0.63\,U_\infty$ and one backward with a higher absolute value. The downstream propagation velocity value is slightly higher than the convective velocity computed in figure 10 to which it is related through Rossiter's model. The upstream velocity u_{up} corresponds to the crossing of pressure waves with an angle α between their propagation direction and the horizontal line used to compute the frequency–wavenumber spectrum. Assuming that the pressure wave travels at velocity $c+u_m$, the angle α can be estimated, using the mean velocity approximation $u_m\simeq 140\,\mathrm{m\,s^{-1}}=0.51\,U_\infty$ that holds on the line $z/D=0$, equal to about 35°, which agrees correctly with the pattern observed in figure 1.

5.1.2. *Analysis of the Kelvin–Helmholtz instability dominated region*

Looking at figures 14 and 15, it is clearly confirmed that the initial growth region of the mixing layer, which is governed by the K–H instability, radically differs from its other parts. In order to improve the analysis of this phenomenon, the characteristics of the velocity fluctuations within the K–H frequency band defined above are presented in figure 16. Taking advantage of local spanwise homogeneity of the fluctuations, the integrated K–H energy is computed as:

$$E_V(x)=\frac{2}{D}\int_{-0.25\,D}^{0.25\,D}\int_{3000}^{6000}\hat{V}(f,x,y,0)^2\,\mathrm{d}f\,\mathrm{d}y,\qquad V=(u,v,w). \tag{5.2}$$

In figure 16(*a*), the energies are normalized using the free-stream velocity. The vertical component is by far the most energetic one in regions where strongly two-dimensional structures are observed. Down at $x/D=0.15$, the other two components have very similar energy levels, but then v' saturates sooner. These results obviously show that the vertical fluctuations are enhanced by a forcing mechanism.

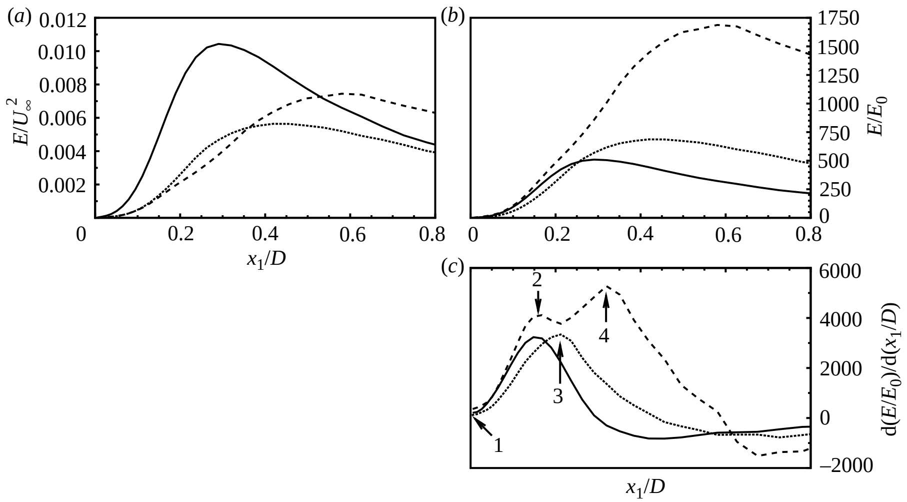

FIGURE 16. Evolution of the characteristics of the K–H instability frequency bands: (*a*) energies contained inside the band normalized by U_∞^2, (*b*) energies contained inside the band normalized using their levels at origin and (*c*) spatial variation rate of energy contained inside the band; — — —, u; · · ·, v; ——, w.

As the K–H instability acts as a noise amplifier because of its convective nature within the range of parameters considered in the present study (Huerre & Rossi 1998), it is of interest to normalize the energy levels using their values E_0 at the origin of the mixing layer. The resulting plots are displayed in figure 16(*b*). Using this reference, the energy increases in the initial region for vertical and longitudinal fluctuations scale almost identically, as expected for two-dimensional K–H instability. However, note that the energy grows with respect to x scales like $\mathrm{e}^{\alpha\sqrt{x}}$ rather than $\mathrm{e}^{\alpha x}$ as predicted by linear theory. This may be due to the residual non K–H related energy lying in the considered frequency band since the flow is already turbulent (because of the incoming boundary layer and the recirculating flow). The transverse fluctuations evolve quite similarly to the w' with a small shift in the downstream direction.

The shift is more clearly discernible in figure 16(*c*), where the energy spatial growth rate evolutions are drawn: one almost identical maximum growth is reached for w' and v', but delayed in the latter case (see in figure 16(*c*), (ii) versus (iii)). On the contrary, two local maxima ((ii) and (iv)) exist for the longitudinal fluctuating energy. The first one occurs in the same location as for w'. Noting that this location corresponds to the maximum time correlation in figure 9, the emergence of two-dimensional structures and the concordance between the frequency predicted by linear stability analysis and the observed one, it appears that location (ii) corresponds to the maximum of purely K–H related energy. The shift between the maxima (ii) for the lines (u',w') and (iii) for the v' line is then interpreted as the delay to transfer energy into the third dimension. Classically, the mechanism involved for such energy transfer is the secondary K–H instability (see for instance Huang & Ho 1990). However, no spectral evidence of such an instability is found. The secondary K–H instability is inhibited, presumably under the influence of the three-dimensional turbulent structures coming from the boundary layer and/or the recirculating flow. Under those circumstances, the transverse fluctuations seem rather to originate from the progressive distortions of the two-dimensional K–H vortices induced by the existence of three-dimensional coherent structures.

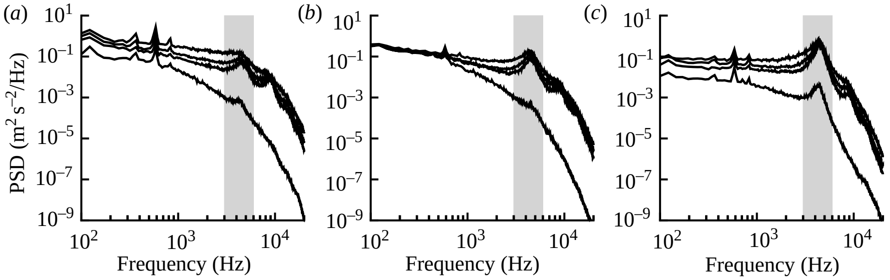

FIGURE 17. Velocity spectra for (*a*) u, (*b*) v and (*c*) w: for each velocity component, the lowest to the highest level spectrum correspond to the locations (i) to (iv) highlighted in figure 16(*c*). Grey bands correspond to the K–H frequency band [3000 Hz, 6000 Hz].

The second peak in the u' line (iv) appears not to be related to the K–H instability. To explain this, the u', v' and w' spectra at each of the locations labelled in figure 16(*c*) are presented in figure 17(*a–c*), with the K–H frequency band highlighted. It is observed, looking at the u' spectra, that between (ii) and (iv), the energy contained in the K–H band increases mainly because of the progressive filling up of the spectrum through the turbulent cascade mechanism. Thus, the evolution of the u' energy spatial growth rate corresponds to a competition between a decreasing K–H instability responsible for peak (ii) and an increasing turbulent cascade yielding peak (iv). A similar competition exists for the two other velocity components, but the K–H peak emerges more clearly from the turbulent background At least two reasons could explain the faster filling of the u' spectrum. First, low-frequency u' energy largely increases between (i) and (iv). Remarking that a similar though less marked growth occurs for w' contrary to v', it is advocated that Rossiter pressure mode forcing is responsible for the energy injection. Secondly, harmonic peaks progressively rise near frequencies $2 \times f_{K-H}$ and $3 \times f_{K-H}$, especially in u' spectra. Similar nonlinear upper harmonics have been observed experimentally (see for instance Miksad 1972) for forced mixing layer, generally related to nonlinear interactions between primary and secondary K–H structures (Huang & Ho 1990). Since there is no evidence of the existence of secondary K–H vortices, the presumed nonlinear interactions observed in the spectra of figure 17 must be analysed to understand better the reinforcement of the small-scale energy.

Bispectral analysis is the preferential tool to study quadratic interactions between time series $X(t)$, $Y(t)$ and $Z(t)$ (see for instance Helland, Van Atta & Stegun 1977, for an application within the turbulence field). Following Kim & Powers (1979), its normalized magnitude, the (squared) bicoherence can be estimated as:

$$Bic^2_{XYZ}(f_1, f_2) = \frac{|\langle \hat{X}(f_1)\,\hat{Y}(f_2)\,\hat{Z}^*(f_1+f_2)\rangle|^2}{\langle|\hat{X}(f_1)\,\hat{Y}(f_2)|^2\rangle\,\langle|\hat{Z}(f_1+f_2)|^2\rangle}. \tag{5.3}$$

Significant levels of bicoherence is an indication of quadratic coupling and the spectra of figure 17, which do not involve a very broadband process, should help in interpreting the results. According to Haubrich (1965) and Elgar & Guza (1988) the 99% significance level for true zero bicoherence using the estimator (5.3) is $Bic^2_{99\%} \gtrsim 9.2/\nu$, where ν is the number of degrees of freedom, here equal to twice the number of blocks used in the average process E[.]. The time series being split into 48 overlapping blocks and the partial homogeneity of the flow in the transverse direction allowing an additional averaging over 50 points, the bound value is found to

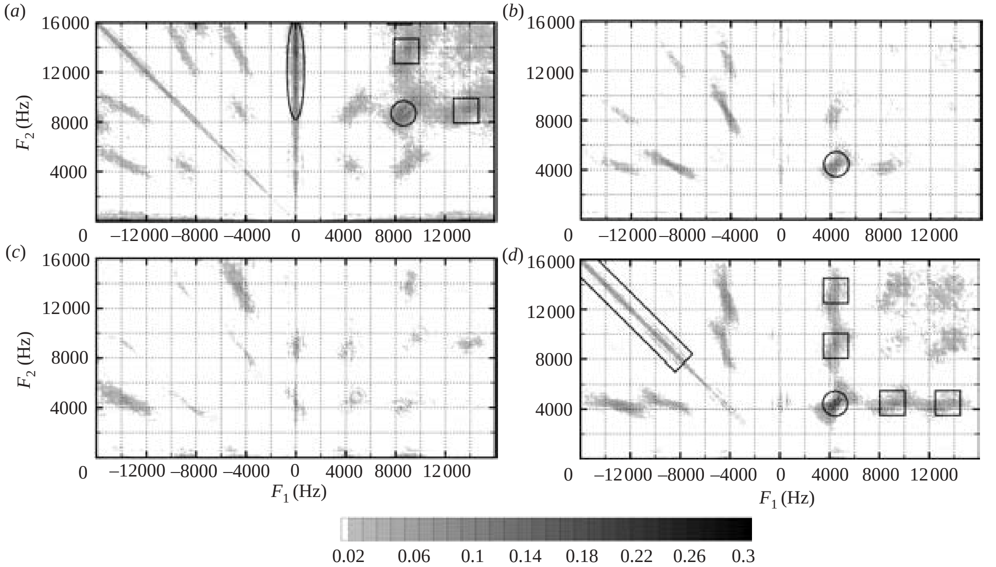

FIGURE 18. Bicoherence spectra at location $x/D = 0.15$ ((ii) in figure 16*c*): (*a*) Bic^2_{uuu}, (*b*) Bic^2_{www}, (*c*) Bic^2_{uuw} and (*d*) Bic^2_{wwu}. Areas surrounded by circles exhibit levels higher than 0.15, as rectangular demarcations denote levels from 0.1 to 0.15.

be 2×10^{-3}. Since transverse points are partially correlated, this value is presumably underestimated and only values at least ten times higher are plotted on the coherence spectra at location $x/D = 0.15$ that are presented in figure 18.

From figure 18(*a*), it is seen that high u auto-bicoherence levels are found on the one hand for $f_1 \simeq 8800$ Hz and f_2 being an harmonic of 4400 Hz and on the other hand for f_1 belonging to the Rossiter mode band $\pm[100\,\text{Hz}, 600\,\text{Hz}]$ and $f_2 \gtrsim 8800$ Hz. For w auto-bicoherence in figure 18(*b*), the only significant level is encountered for frequencies $f_1 = f_2 \simeq 4400$. Figures 18 (*c*) and 18 (*d*) are dedicated to cross-bicoherence. From the first one, it is seen that there is almost no quadratic interaction between uu and w. In contrast, the second one reveals multiple significant triadic interaction areas between ww and u. The highest level of nearly 0.3 is encountered for $f_1 = f_2 = 4400$ Hz. Because of the difference in spectral energy levels between $\hat{w}(4400\,\text{Hz})$ and $\hat{u}(8800\,\text{Hz})$, it appears that this interaction is responsible for the 8800 Hz peaks in the spectra of figure 17. Other lower, but still significant, bicoherence levels are found between harmonics of 4400 Hz for both u and w as well as between broadband high frequencies for w and Rossiter modes for u. For the first interaction, the autospectra do not allow us to determine the direction of the energy transfer. For the second one, energy is more likely to be transfered from u to w because of the large energy gap. Moreover, it could be interpreted as a consequence of a linear correlation between u' and w' for high frequencies with, formally, the already mentioned nonlinear transfer from Rossiter mode bands to high frequencies for u, followed by linear interaction between u and w. This hypothesis holds since significant levels of (linear) squared coherence between u and w are found for the frequency regions in the vicinity of 8800 Hz and 13 200 Hz, as seen in figure 19. Eventually, it is worth noting that no bicoherence involving transverse velocity is presented because it leads to uniformly non-significant levels. Therefore, as for the K–H frequency band, harmonic peaks that exist in v' spectra are believed to be due to three-dimensional

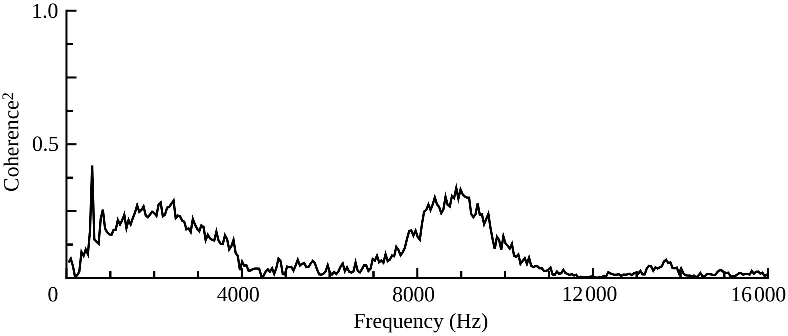

FIGURE 19. Squared coherence inside the mixing layer between streamwise and vertical velocity at location $x/D = 0.15$.

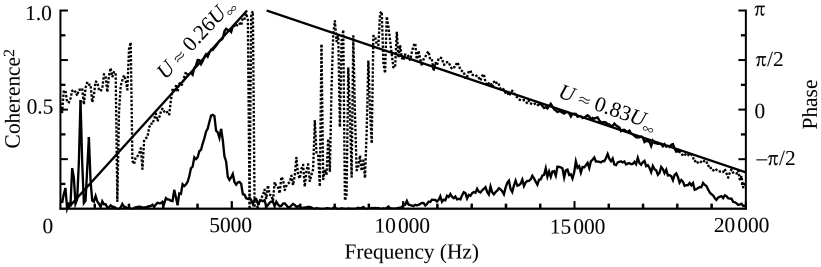

FIGURE 20. Cross-spectrum inside the mixing layer between vertical velocity at $x/D = 0.015$ ((i) in figure 16*c*) and pressure at $x/D = 0.15$ ((ii) in figure 16*c*): ——, squared coherence; · · ·, phase.

energy redistribution through either pressure waves or distortions of two-dimensional structures.

Using the aforementioned information coming from velocity spectra, cross-spectra and bispectra of figures 17 to 19 , the scenario for the energy budget of the mixing layer at its early stage could be summarized as follow:

(i) The vertical velocity component w is subject to an initial forcing at frequency $f_{for} \simeq 4400$ Hz.

(ii) Through nonlinear interactions, energy is transferred from $\hat{w}(f_{for})$ toward $\hat{w}\,(2 \times f_{for})$.

(iii) A quadratic cascade process initiates for u from $2 \times f_{for}$ to higher harmonics of f_{for} which are also partially fed by triadic interaction with the low-frequency highly energetic Rossiter modes.

(iv) Mostly because of linear interactions, energy from the small scales of u is transferred to the small scales of w, jointly with a auto nonlinear transfer originating from $\hat{w}(f_{for})$.

Once the nonlinear analysis of the mixing layer has been performed, the open problem of the origin of the forcing upon the vertical velocity component w still remains. First, we have to check that it is not simply related to a distant influence of the developed K–H instability because of upstream travelling pressure waves. This hypothesis is investigated through the analysis of the cross-spectrum between p at location $x/D = 0.15$ and w near the origin of the shear layer ($x/D = 0.015$) presented in figure 20. Three bands of high squared coherence are seen, including the

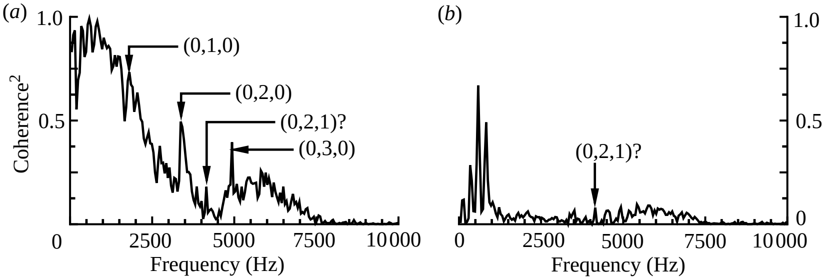

FIGURE 21. Cross-spectrum inside the mixing layer between the floor of the cavity and the mixing layer at location $x/D = 0.015$: (*a*) pressure–pressure squared coherence and (*b*) pressure–vertical velocity squared coherence.

K–H one. However, the phase spectrum reveals that this last-mentioned corresponds to a downstream convection with a phase velocity equal to the local convective velocity found in figure 10. Nonetheless, note the upstream oriented influence for high frequencies owing to the excitation of the initially low energetic w' small scales by the pressure waves emitted by the structures created downstream through nonlinear interactions.

Since the forcing acts preferentially on the vertical velocity, one other possibility is that it is related to an acoustic cavity mode including a vertical component. Unfortunately, time series have not been stored for the vertical walls. However, we can compute a cross-spectrum between the floor of the cavity and the mixing layer. Figure 21 shows the squared coherence at location $x/D = 0.015$ between p on the floor of the cavity and, respectively, p (figure 21*a*) and w (figure 21*b*) inside the mixing layer. From figure 21(*a*), apart from the Rossiter modes, three peaks of high coherence labelled (0,1,0), (0,2,0) and (0,3,0) are detected. They correspond to transverse acoustics modes, as will be demonstrated in § 5.2, with their frequencies agreeing with the theoretical frequencies of the acoustic proper modes of a cavity with five rigid walls and a top open end. Two such acoustic modes with a non-zero vertical number yield frequencies lying within the K–H band: $f_{0,2,1} = 4150\,\mathrm{Hz}$ and $f_{0,1,2} = 4370\,\mathrm{Hz}$. No peak corresponding to the latter frequency appears, but one with a frequency equal to 4160 Hz exists both for p–p and p–w bicoherence. However, the coherences observed at its frequency are too low to explain completely the forcing observed on w.

5.2. *Pressure on the floor of the cavity*

5.2.1. *Global analysis*

The very same spectral analysis carried out in § 5.1.1 but restricted to pressure is applied to the floor of the cavity. Figure 22 presents the evolution of the pressure spectra for the two streamwise lines $(y/D, z/D) = (0, -1)$ (figure 22*a*) and $(y/D, z/D) = (0.25, -1)$ (figure 22*b*). Concerning the Rossiter modes, we can see a strong modulation of mode amplitude with respect to the streamwise location, independent of the spanwise location. A global almost exponential decrease of the base levels between the aft and fore walls is also observed on the two parts of the figure. The main difference between the two plots appears to be the existence of different peaks above the Rossiter mode frequency area: about 3400 Hz and 6350 Hz for the centreline and nearly 1800 Hz, 4850 Hz and 6350 Hz for the quarter-width line. Note that such peaks generally persist over the whole streamwise range.

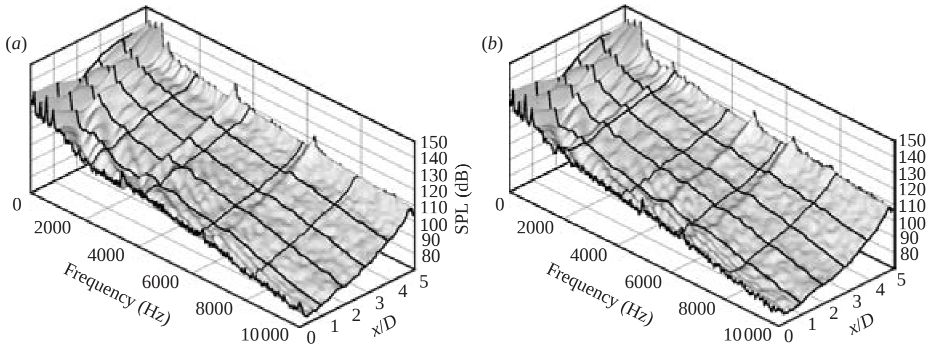

FIGURE 22. Spectral surfaces of pressure fluctuations along the longitudinal direction on the floor of the cavity: (*a*) line $y/D = 0$ and (*b*) line $y/D = 0.25$.

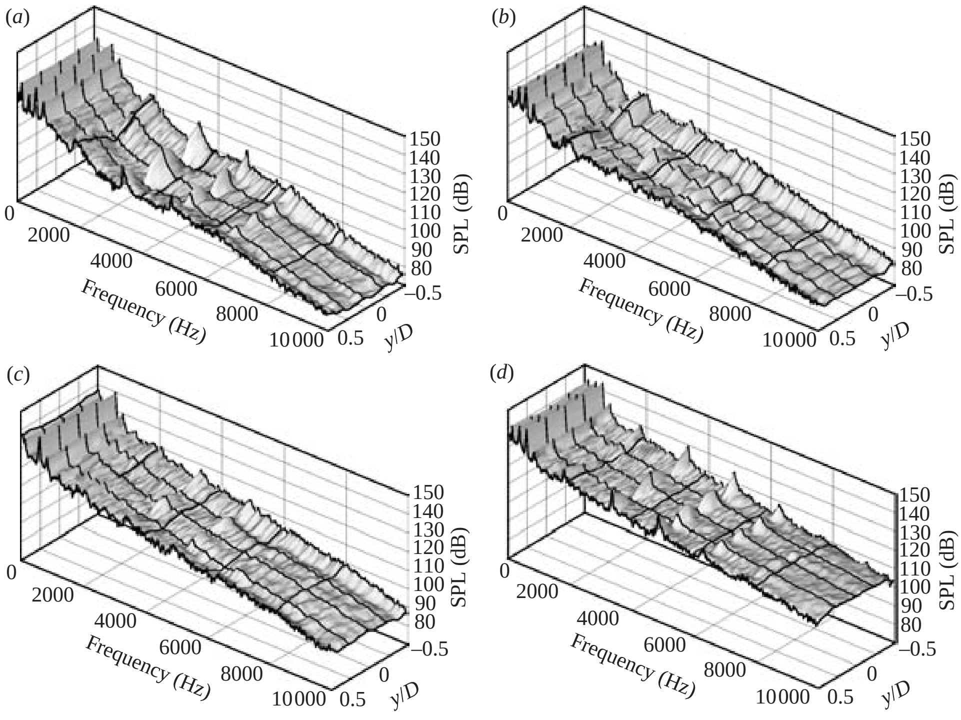

FIGURE 23. Spectral surfaces of pressure fluctuations on the floor of the cavity at four different locations on the x-axis corresponding to locations (*a*) $x/D = 0.25$, (*b*) $x/D = 1.75$, (*c*) $x/D = 3.25$ and (*d*) $x/D = 4.75$.

In addition to streamwise spectra, the evolution of pressure spectra along the span is presented in figure 23 at four streamwise locations. Such plots first reveal an even more two-dimensional behaviour of the Rossiter modes on the floor of the cavity than inside the mixing layer. The non-Rossiter-related peaks are also recovered and exhibit very regular spanwise patterns which allows us to conclude that such peaks correspond to transverse acoustic modes. The differences mentioned when studying

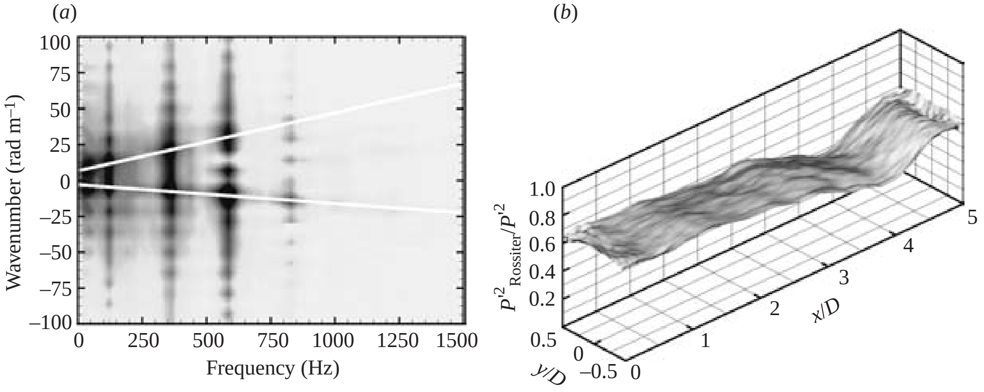

FIGURE 24. (*a*) Frequency–wavenumber pressure spectrum along the line ($y/D = 0, z/D = -1$) and (*b*) pressure fluctuations on the floor related to Rossiter mode frequency band normalized using the local total pressure fluctuation value.

the two parts of figure 22 are consequently explained by the location of the nodes and anti-nodes of such modes.

As previously mentioned in § 5.1.2, the frequencies of the above-highlighted spanwise acoustic modes are predicted well using the theoretical formula related to the proper mode of a cavity at rest with one open end. The fundamental (0,1,0) and the first harmonic (0,2,0) are the dominant modes, and higher harmonics (0,3,0), (0,4,0) and even (0,5,0) are reinforced in the vicinity of the wall.

5.2.2. *Rossiter modes*

In the same way as figure 15 for the mixing layer, figure 24(*a*) exhibits phase velocity, and figure 24(*b*) amplitude information related to the Rossiter modes on the floor of the cavity. From figure 24(*a*), two phase velocities are observed: the upstream propagation at velocity u_{up} corresponds to pressure waves travelling with velocity equal to the speed of sound c. By neglecting the reverse flow, the velocity u_{up} observed on the floor line allows us to estimate the angle α between the wave front and the floor as nearly equal to $\alpha \simeq 45°$. The downstream component value is related to pressure waves emitted by the vortical structures of the layer and travelling almost vertically down to the floor. Concerning figure 15(*b*), we observe that the sum of Rossiter mode energy levels normalized by the local value of p'^2 is higher than inside the mixing layer: the Rossiter modes globally contribute for a constant value of 60% to the total p variance, except around $x/D = 4$ where the contribution drops to 40%.

The study of the individual Rossiter modes band-integrated energy presented in figure 25 allows us to explain this feature. The energy level related to each of the Rossiter modes exhibits nodes with respect to the x-coordinate. Therefore, the drop in the total Rossiter mode energetics contribution around $x/D = 4$ is a consequence of the existence of nodes for modes 2 to 4 in the close vicinity of that location. We may remark that very similar mode shapes have already been reported for closely related experimental configurations ($L/D = 4$ and $M = 0.8$, see Heller & Bliss 1975). They also bear some resemblance to cavity acoustic proper mode subject to exponential damping.

According to Ahuja & Mendoza (1995), the shapes of the modes are due to a complex combination of the pressure related to mixing-layer instability waves and

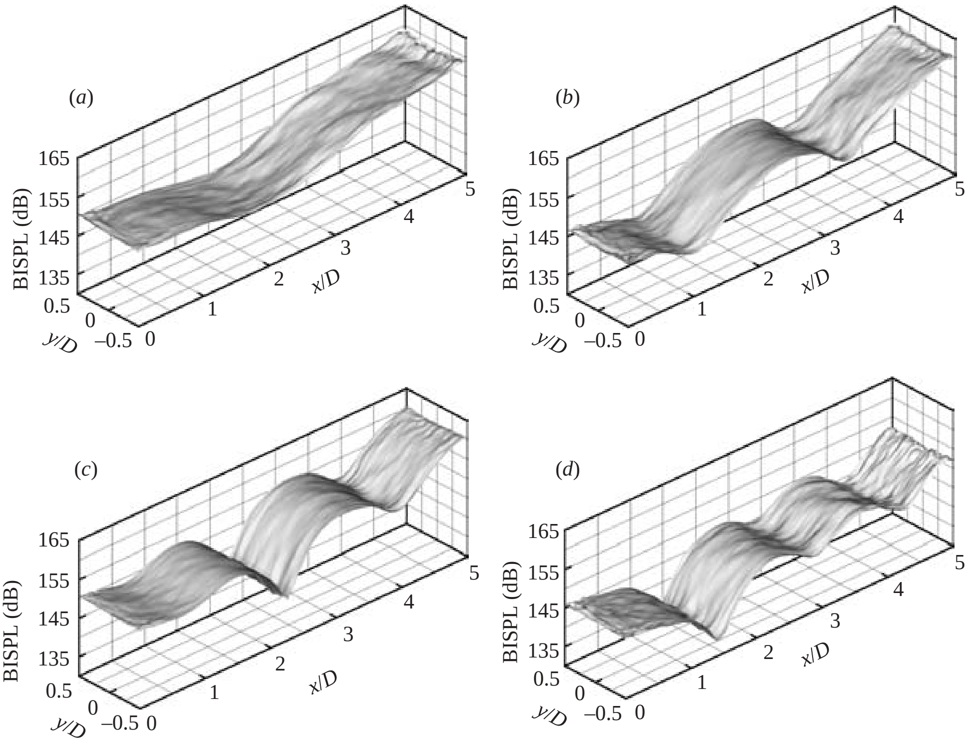

FIGURE 25. Band integrated SPL for Rossiter modes: (*a*) first mode, (*b*) second mode, (*c*) third mode and (*d*) fourth mode.

the acoustic pressure waves, as observed also for upstream tone excited jets. Tam & Morris (1985) have modelled this 'receptivity problem' by means of a quasi-linear formulation. They show that for such an interaction to occur requires that the two kinds of wave are of comparable amplitude, the wavelength of the observed pattern being approximatively equal to that of the mode with the shortest wavelength. In the present case, the amplitude hypothesis is indeed verified in the initial region of the mixing layer, as can be seen in figure 13(*a*), but beyond, there is no further evidence of energetic K–H instability. Moreover, the modulation by the wavelength of a single instability could hardly explain the reducing wavelength of the shape pattern as the mode number increases. Nevertheless, downstream-travelling vortices could play a role similar to instability waves, and their theoretical wavelength $\lambda_\omega = \kappa U_\infty / f$ could correspond. Note that such distinction between short- and long-wavelength instability waves has already been highlighted in high-Reynolds-number cavity flow (Lin & Rockwell 2001).

To validate the hypothesis concerning the origin of the shape of the mode, we can suppose, in the same way as Rossiter's model and following Heller & Bliss (1975), that the pressure modes on the floor of the cavity can be modelled as the sum of two plane pressure waves with the same amplitude: a downstream propagating one related to the coherent structures in the mixing layer, as their pressure traces are observed even on the floor (see figure 24), and an upstream propagating one. White noise (*WN*) is then added so has to mimic some effects of the turbulent background

Mode number i	1	2	3	4
α_i	11.004	10.524	11.236	10.021
β_i	4.278	6.492	5.058	4.821

TABLE 5. Coefficients issued from the fitting of the Rossiter mode amplitude.

flow, and the proposed model for pressure fluctuation reads:

$$p(x,t)=\sum_{i=1}^{4} A_i(x)\left\{\cos\left[2\pi f_i\left(\frac{x}{u_+}-t\right)+\Phi\right]+\cos\left[2\pi f_i\left(\frac{x}{u_-}-t\right)\right]\right\} \\ +A_{WN}(x)\ WN(x,t), \tag{5.4}$$

where $A_i(x)$ and f_i are the amplitudes and frequencies of the Rossiter modes, u_+ and u_- are the velocity of the downstream and upstream travelling waves, Φ is the phase shift between the two kinds of waves at origin and $A_{WN}(x)$ is the amplitude of the added white noise $WN(x,t)$.

In order to obtain an accurate evaluation of the proper shape of the square of the Rossiter modes, we have to remove the contribution of the base level to the band-integrated energy. This is performed by both assuming that the spectral density at the two bounds of a band is free from energy coming from the corresponding Rossiter mode and that there is a linear evolution of the base level between these bounds. Then, taking into account the two-dimensionality of the Rossiter modes seen in figure 25, the span smoothed E_{R_i} corrected energy due to each modes reads:

$$E_{R_i}(x)=\frac{1}{W}\int_{-0.5W}^{0.5W}\left\{\int_{a_i}^{b_i} S_{pp}(f,x,y)\,\mathrm{d}f-\frac{b_i-a_i}{2}\left[S_{pp}(a_i,x,y)+S_{pp}(b_i,x,y)\right]\right\}\mathrm{d}y, \tag{5.5}$$

where a_i and b_i are, respectively, the lower and upper bounds of the frequency band related to the ith Rossiter mode. The values for the $A_{i=1,\ldots,4}$ are obtain by a least-squares fitting of the resulting shape using the functions $A_i(x)^2/2=\exp(\alpha_i+\beta_i\,x)$, thus leading to the coefficients in table 5, and $A_{WN}(x)^2$ is computed so as to correspond to 40% of the $\sum_i A_i(x)^2$, as seen in figure 24. According to figure 15, $u_+=175\,\mathrm{m\,s^{-1}}$ and it is assumed that the velocity of the upstream travelling waves is the speed of sound on the floor of the cavity, i.e. $u_-=-340\,\mathrm{m\,s^{-1}}$.

From table 5, we can see that the damping rate is very similar for modes 1, 3 and 4 and slightly higher for mode 2. We can therefore use this kind of similarity to obtain the normalized mode shapes by dividing the energy level of a mode by the sum over all the modes of the energy levels. Such a normalization allows us to obtain a convenient plot for the shape of the mode, as seen in figure 26(a), which clearly highlights a local highly symmetric pattern with respect to the location $x/D\simeq 2.3$. The last parameter of the model, namely Φ, which acts by globally shifting all the proper shapes in the streamwise direction, is therefore adjusted so as to obtain the same quasi-symmetry axis location, resulting in $\Phi/2\pi=0.33$. Note that for Rossiter's model, there is a phase shift at the end of the cavity rather than at the origin. However, the value of $\Phi/2\pi=0.33$ is close to $\gamma=0.29$ of Rossiter's model for $L/D=5$. Finally, the phase shift can be seen as a way to take into account the far from constant velocity of the structures in the beginning of the shear layer. Therefore, the model is not expected to behave well near the fore wall.

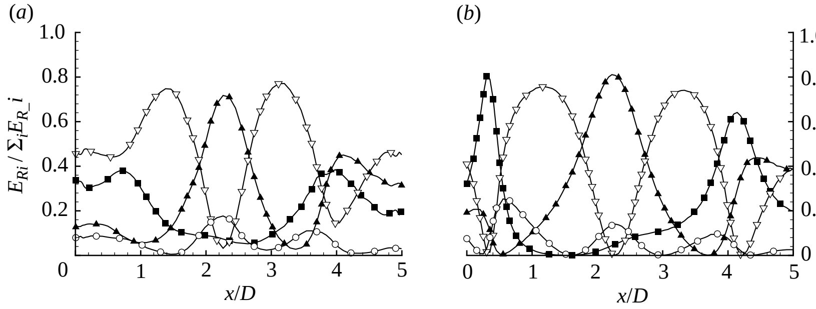

FIGURE 26. Normalized squared Rossiter proper modes shape from (*a*) the computation and (*b*) model (5.4): ■, first mode; ▲, second mode; ▽, third mode; ○, fourth mode.

The normalized squared shape found from (5.4) and the above set parameters are plotted in figure 26(*b*). As postulated, the results are not good for the beginning of the cavity. Nonetheless, the agreement with the measurements is very favourable in the region $1.25 < x/D < 4$, with an accurate prediction of both the relative amplitudes and node/anti-node locations except for a node shifted to the left for mode 1. However, it is advocated that mode 1 yields the less measured-wave characteristic shape, presumably because of the interactions with low-frequency large hydrodynamic structures. The model does not allow us to obtain a non-zero fluctuation node, contrary to what it is observed from the simulation results for mode 3 at location $x/D = 2.3$. Consequently, the relative amplitudes of the anti-node for mode 2 are slightly over-evaluated. Nonetheless, an imperfection of the procedure used to remove the base level of the pressure spectrum near the peak frequencies could be responsible for such a non-zero node level. Above $x/D = 4$, a marked non-zero node for mode 3 occurs, largely altering the predictions of the relative amplitudes, but the node locations are still correctly recovered.

To conclude this study of the Rossiter modes on the floor of the cavity, it is of some interest to check possible non-linear interactions between modes, as highlighted by Rockwell & Knisely (1980) for incompressible case and Kegerise *et al.* (2004) for subsonic inflow conditions. This is performed through the use of bispectral tools, as for velocity inside the mixing layer. However, the narrower frequency bands of interest require us to increase the size of the FFT data block so as to increase the spectral resolution, and therefore to reduce the number of averaging blocks, leading to an increased level of uncertainty. To partially compensate for this drawback, the FFT results are averaged for the 100 span points instead of 50 previously retained by taking advantage of the two-dimensionality of the Rossiter modes. Since the span points are highly correlated, the significance level for true zero bicoherence must be multiplied by a factor of three compared to the previous analysis.

The resulting auto-bicoherence spectra are presented in figure 27 for two locations in the vicinity of the walls, where the highest levels are. Globally, significant nonlinear coupling is observed for almost each couple of Rossiter mode frequencies. The highest values are found for the interaction of mode 3 with itself: 0.26 near the fore wall (figure 27*a*) and 0.22 near the aft wall (figure 27*b*). Such maximal values lie between those observed experimentally by Kegerise *et al.* (2004): higher bicoherence values of 0.55 if the sum (or difference) of two mode frequencies matches a third mode frequency and lower bicoherence values of nearly 0.15 if not, as in the present case. Lower levels of nearly 0.20 are encountered for couplings between mode 3 and mode (−1)

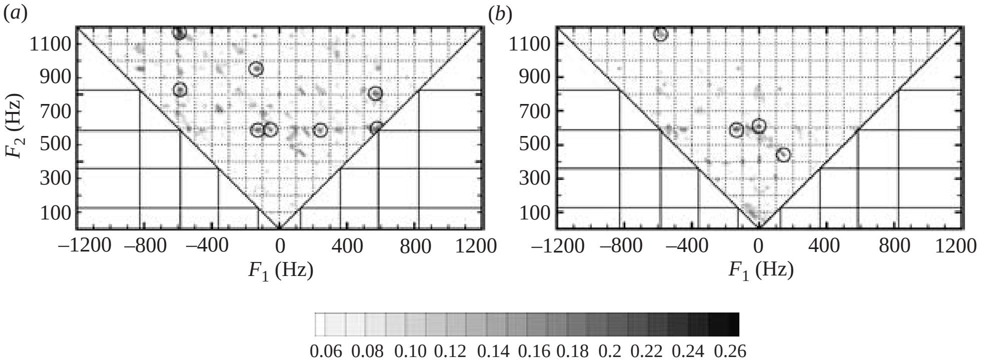

FIGURE 27. Auto-bicoherence spectra for pressure on the floor of the cavity at locations (*a*) $x/D = 0.015$ and (*b*) $x/D = 4.985$. The squared bicoherence levels higher than 0.20 are surrounded by a circle, and the solid lines corresponds to Rossiter mode frequencies.

(figure 27*a* and *b*) and mode (−3) with mode 4 (figure 27*a*). They could be responsible for the small bumps observed here and there near 250 Hz and 450 Hz in figure 5. There are also high levels of bicoherence for an interaction between mode 3 and frequencies lower than 50 Hz. Note that, similar to the observations made by Kegerise *et al.* (2004), these low-frequency bicoherence components do not correspond to the sum or difference of Rossiter mode frequencies. They could be related to a modulation of the Rossiter modes by large-scale flow structures; see for instance Lin & Rockwell (2001) for an example of such a modulation.

5.3. *Joint time–frequency analysis of the Rossiter modes*

From the joint analysis of the experimental and computed pressure spectra, there is some evidence that the pressure signal is not strictly stationary. Some other studies have already observed such behaviour, characterized either by a temporal variation of the frequency of the mode (jitter effect, see Forestier *et al.* 2003; Larchevêque *et al.* 2003) or a period to period variation of the dominant Rossiter mode (‘mode switching’, Kegerise *et al.* 2004). Two ways have been used to characterize such variations. The first relies on the rapid schlieren visualization of the number of large vortical structures that exist in the core of the mixing layer. However, as can be verified by phase averaging (Forestier *et al.* 2003; Larchevêque *et al.* 2003), there is not always a direct relation between the mode number and the number of vortices that are discernible at a given time. Moreover, this approach can be biased if two modes of similar amplitude exist in the same time interval.

Another less empirical way is to use joint time–frequency spectral analysis of the data. One of the simplest tools for achieving such analysis is to use the so-called short-time Fourier transform (STFT) inspired by the work of Gabor (1946). The STFT of a given signal $p(t)$ reads:

$$\mathrm{STFT}(t, f) = \int_{-\infty}^{+\infty} p(\tau)\, w(\tau - t) \mathrm{e}^{-\sqrt{-1}\, 2\pi f \tau}\, \mathrm{d}\tau, \tag{5.6}$$

where $w(t)$ is a sliding temporal window function. Because of the uncertainty principle which states that $\Delta t \times 2\pi \Delta f \geqslant 1/2$, we have to make a compromise between temporal and spectral resolution. In the present study, we have chosen to consider a time interval corresponding to two periods of the lower Rossiter modes, which leads to a 1666 point segment with a sampling rate of 100 kHz. The resulting discrete Fourier transform

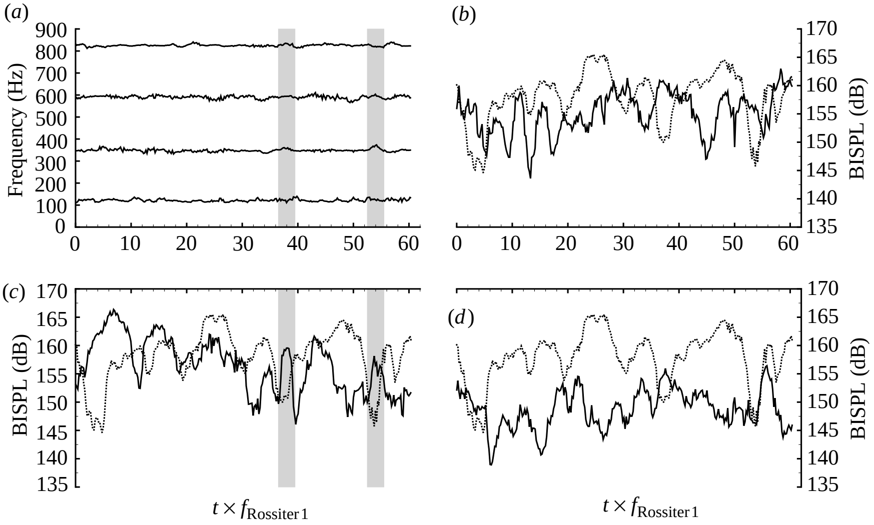

FIGURE 28. Time–frequency analysis of the pressure signal at location $x/D = 4.985$. Evolution of frequencies of the four Rossiter modes (*a*), and comparison between the BISPL levels of mode 3 (dotted, *b–d*) and mode 1 (solid, *b*), 2 (solid, *c*) and 4 (solid, *d*). The time is normalized using the duration of one period of the first Rossiter mode and grey bands highlight periods of 'mode switching' between the second and third modes.

therefore corresponds to a frequency resolution of 60 Hz, which requires a STFT time step greater than 1.3 ms. It has therefore been fixed at 1.66 ms, corresponding to 90% overlapping successive segments. However, with such a large-frequency resolution, is is difficult to discriminate Rossiter mode energy as for the BISPL technique.

Our solution for partially overcoming this problem is to use a Burg estimator rather than a traditional FFT one. As has been mentioned previously, such an approach makes it possible optimize, in some mathematical sense, the frequency locations of the points that describe the spectrum shape, without formally increasing the spectral resolution. In a stationary Burg spectral analysis, no window is applied beforehand to the signal (which formally corresponds to a square window), contrary to classical FFT-based estimators. It has therefore been decided to maintain this characteristic by using a square sliding temporal window $w(t) = \mathrm{I}_{[-1/f1,1/f1]}(t)$. Since a Burg estimator is parametric, the order of the model (number of poles) has to be determined. Based on some tests, it has been set to a fifth of the number of points in the data segment. Analogously, the time-frequency spectral estimator defined in that way is hereinafter referred to as a short-time Burg transform (STBT).

To obtain the energy levels corresponding to each Rossiter mode, the same procedure as for the stationary analysis is used, relying on the integration of the pressure spectra over the frequency bands given in table 3. The frequency of the mode is then estimated as the frequency of the energy centroid over the related band.

Figure 28 illustrates the results of the process for a location where significant low-frequency nonlinear interactions were observed in § 5.2.2. From figure 28(*a*), it is seen that there are only small temporal evolutions of the frequency of the modes. On the contrary, figure 28(*b–d*) shows that the levels of the mode are significantly time modulated. For modes 1 and 3, the amplitudes in the variation of the level are close to 10 dB, when they are approximatively equal to 7.5 dB and 5 dB for mode 2 and 4, respectively. These modulations are fully spanwise correlated and the Fourier

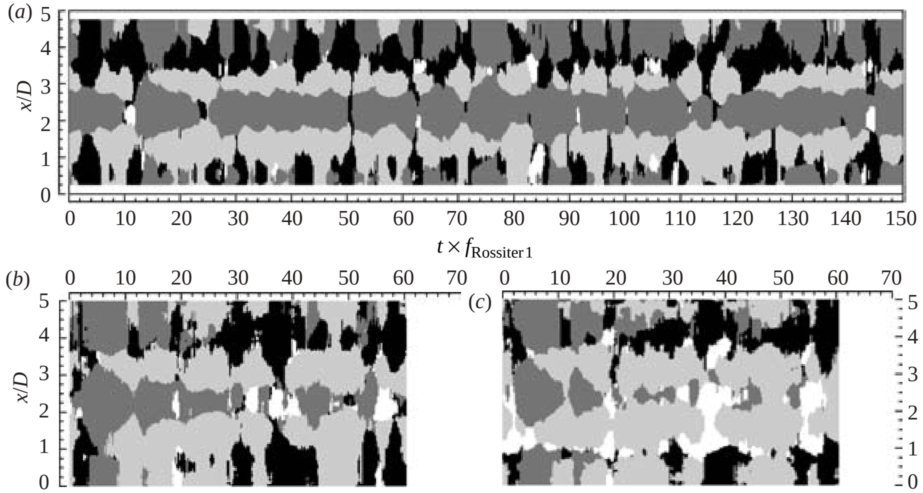

FIGURE 29. (a) Time–space evolution of the dominant Rossiter mode interpolated from the ten streamwise experimental measurement locations on the floor of the cavity and (b) issued from the LES on the floor of the cavity and (c) inside the mixing layer: black, mode 1; dark grey, mode 2; light grey, mode 3; white, mode 4. The time is normalized using the duration of one period of the first Rossiter mode.

transforms of the mode level time series exhibit very low-frequency components between 5 and 35 Hz, independently of the streamwise location considered. For the third Rossiter mode in particular, two marked enharmonic peaks at frequencies 7.5 Hz and 15 Hz are encountered. Such low-frequency modulations could therefore explain the high bicoherence levels involving low frequency and the third Rossiter mode that are observed in the pressure bispectra. Also note that the frequencies seem too low to correspond directly to a modulation by large-scale hydrodynamics, whose frequency estimated from the recirculation inside of the cavity scales like 40 Hz.

Figure 28 also underscores 'mode switching' between modes 2 and 3 for times $t^* = t \times f_{\text{Rossiter}_1} \simeq 38$ and $t^* \simeq 54$ that are highlighted by grey bands: for duration of about three periods of the first Rossiter mode, the level of mode 3 drops as the level of mode 2 increases in return. Conjointly, the frequency of the second mode tends to be slightly shifted upwards. Note that for other locations, 'mode switching' between modes 1 and 3 is also observed.

Because of the 'mode switching', it is of interest to consider the concept of dominant mode, classically defined as the mode with the highest inner energy. By taking advantage of the spanwise independence for the level of the modes time series, we are able to draw a time–space map of the dominant Rossiter pressure mode at specified time and streamwise location. Such maps are displayed for the experimental measurements in figure 29(a) and for the LES on the floor of the cavity and inside the mixing layer in figures 29(b) and 29(c), respectively. Note that the experimental map is computed from the only ten available streamwise locations and then interpolated for the other ones, thus leading to areas with smooth boundaries. Nonetheless the comparison of figures 29(a) and 29(b) shows good agreement for the streamwise and unsteady dominant mode evolution between the experiment and the LES. The differences are mostly due to the small discrepancies mentioned in § 3.2: slightly over-evaluated modes 1, 2 and 4 and slightly under-evaluated second mode. For both maps, temporal variation of the dominant mode over several periods of the first

Rossiter mode are observed. We are therefore able to conclude that for the class of cavity flow where several Rossiter modes with close peak levels coexist, the concept of dominant mode is quite irrelevant because of its space modulation and above all its temporal variability over large duration due to the ‘mode switching’. Finally note that, as expected, the comparison of the dominant mode maps issued from the floor of the cavity and the mixing layer shows that, despite different spatial distribution, the temporal modulations for the levels of the Rossiter modes are quite synchronized over the whole cavity volume.

6. Synthesis and conclusions

Large-eddy simulations of a high-Reynolds-number three-dimensional cavity flow have been carried out.

The comparisons of the numerical results with the experimental pressure measurements for the very same configuration demonstrate very good agreement. It includes the prediction of the spectrum peak level with an error lower than 5 dB for each of the locations tested and the recovery of the correct cross-spectra information (phase and coherence) between the probes. Such meticulous validation procedure allows therefore a high level of confidence concerning the numerical data that cannot be compared with experiments because of unavailable velocity data.

Concerning the mixing layer, two regions have been identified along the cavity length. First, a Kelvin–Helmholtz zone that extends over one sixth of the cavity and can itself be decomposed into several sub-regions. Initially, in contrast with a free mixing layer, narrow-band vertical velocity fluctuations prevail over streamwise and spanwise ones in the very vicinity of the fore wall and this unusual characteristic is seen as the signature of a forcing mechanism at the high frequency of nearly 4500 Hz. Though a depth acoustic mode could be partially involved in the forcing, its origin is not clear.

Then, up to $x/D = 0.15$, energy redistribution between the velocity components occurs. The joint use of cross-spectra to highlight linear energy transfer between identical frequencies, bispectra to demonstrate significant quadratic (triadic) interactions and auto-spectra to determine the direction of the transfer has yielded the following scheme: the initially 4400 Hz vertical fluctuations reinforce the near 8800 Hz vertical fluctuations through triadic interactions. Then streamwise velocity component triadic transfers take place from combinations of 4400 Hz and 8800 Hz frequencies up to higher ones, initiating the turbulent cascade process fed by low-frequency Rossiter-mode-related fluctuations. For the high frequencies, energy is next linearly transfered from the streamwise velocity to the two other components.

The location $x/D = 0.15$ corresponds both to the end of the region where significant quadratic interactions take place, to the coincidence of the forcing frequency with the local most amplified K–H one and to the apparition of mainly two-dimensional spanwise vortical tubes emerging from the three-dimensional turbulent background. The spanwise integral length downstream decreases up to the location $x/D = 0.7$ where the mixing transition is achieved and preferentially two-dimensional structures are no longer seen.

The second region of the layer (between $x/D = 0.7$ and $x/D = 4.8$) is characterized by a behaviour very similar to a free developed shear layer. Its vorticity thickness increases linearly, but it is demonstrated that the recirculating flow has to be considered as soon as the thickness reaches a magnitude similar to the depth of the cavity.

The pressure has been analysed on planes corresponding to the floor of the cavity and the centre of the mixing layer. Whatever the location considered inside these two planes, four peaks whose frequencies below 1000 Hz correctly agree with the Rossiter model prediction are encountered in the pressure spectra. These peaks are responsible for 40% to 60% of the total pressure fluctuation inside the cavity, thus illustrating the turbulent nature of the flow. It is also shown that each peak level is spanwise independent, but is largely modulated in the streamwise direction. By means of a simple two-wave model inspired by Rossiter's interpretation of its semi-empirical model, it is demonstrated that such modulation originates from the interaction between an upstream acoustic wave and a downstream vortical wave of similar amplitude. The correct prediction of frequencies and proper shape by means of models based on the same hypothesis allows us to clarify the concept of Rossiter modes. The pressure bispectrum highlights nonlinear interaction between the third Rossiter mode and very low frequencies. Such low frequencies are also encountered for time modulation of the amplitude of the modes as revealed by joint time–frequency analysis, especially for the third mode. It is also demonstrated from the the experiment and the computation that, for this cavity, the dominant Rossiter mode is both space- and time-dependent.

Apart from the four Rossiter modes, four to five peaks of frequencies higher than 1800 Hz and exhibiting spanwise modulations are observed on the floor of the cavity only. Their frequencies and proper shapes lead us to categorize them as spanwise acoustic proper modes of the cavity.

To conclude, dominant and auxiliary mechanisms for a high-Reynolds-number cavity flow have been identified and analysed. In some future works, it should be of interest to focus on the Rossiter mode intermittency as an improved understanding of their mechanisms could lead to some insights in the control of cavity-flow oscillations. The initial region of the mixing layer also requires further analyses to identify the origin of the forcing mechanism. Note that such analyses could take advantage of the use of high-order spatial schemes to reduce mesh constraints while preserving a high accuracy level. Lastly, the meticulous analysis of high-Reynolds transitional or even non-resonant closed-cavity flow fields should also be considered.

L. L. wishes to thank Dr L. Jacquin and Dr E. Manoha for the fruitful discussions about some aspects of vortices dynamics and acoustic wave analysis tools.

REFERENCES

Ahuja, K. K. & Mendoza, J. 1995 Effects of cavity dimensions, boundary layer, and temperature on cavity noise with emphasis on benchmark data to validate computational aeroacoustic codes. *NASA Contractor Rep.* 4653.

Bilanin, A. J. & Covert, E. E. 1973 Estimation of possible excitation frequencies for shallow rectangular cavities. *AIAA J.* **11**, 347–351.

Block, P. J. W. 1976 Noise response of cavities of varying dimensions at subsonic speeds. *NASA TN* D-8351.

Browand, F. K. & Trout, T. R. 1985 The turbulent mixing layer: geometry of large vortices. *J. Fluid Mech.* **158**, 489–509.

Cattafesta, L. N., Garg, S., Choudhari, M. & Li, F. 1997 Active control of flow-induced cavity resonance. *AIAA Paper* 97-1804.

Childers, D. G. (ed.) 1978 *Modern Spectrum Analysis*, chap. 2, pp. 23–148. IEEE Press, New York.

Colonius, T. 2001 An overview of simulation, modeling, and active control of flow/acoustic resonance in open cavities. *AIAA Paper* 2001-0076.

East, L. F. 1966 Aerodynamically induced resonance in rectangular cavities. *J. Sound Vib.* **3**, 277–287.

Elgar, S. & Guza, R. T. 1988 Statistics of bicoherence. *IEEE Trans. Acoust. Speech Sig. Proc.* **36**, 1667–1668.

Forestier, N., Jacquin, L. & Geffroy, P. 2003 The mixing layer over a deep cavity at high-subsonic speed. *J. Fluid Mech.* **475**, 101–145.

Gabor, D. 1946 Theory of communication. *J. Inst. Electr. Engng Lond.* **93**, 429–457.

Gharib, M. & Roshko, A. 1987 The effect of flow oscillations on cavity drag. *J. Fluid Mech.* **177**, 501–530.

Gloerfelt, X., Bailly, C. & Juvé, D. 2003 Direct computation of the noise radiated by a subsonic cavity flow and application of integral methods. *J. Sound Vib.* **266**, 119–146.

Gloerfelt, X., Bogey, C., Bailly, C. & Juvé, D. 2002 Aerodynamic noise induced by laminar and turbulent boundary layers over rectangular cavities. *AIAA Paper* 2002-2476.

Grace, S. M. 2001 An overview of computational aeroacoustic techniques applied to cavity noise prediction. *AIAA Paper* 2001-0510.

Haubrich, R. A. 1965 Earth noise, 5 to 500 millicycles per second: 1. spectral stationarity, normality and nonlinearity. *J. Geophys. Res.* **70**, 1415–1427.

Heller, H. H. & Bliss, D. B. 1975 The physical mechanism of flow-induced pressure fluctuations in cavities and concepts for their suppression. *AIAA Paper* 75–491.

Heller, H. H., Holmes, D. G. & Colvert, E. E. 1971 Flow-induced pressure oscillations in shallow cavities. *J. Sound Vib.* **18**, 545–553.

Helland, K. N., Van Atta, C. W. & Stegun, G. N. 1977 Spectral energy transfer in high reynolds number turbulence. *J. Fluid Mech.* **79**, 337–359.

Heller, H. H., Widnall, S. E., Jones, J. & Bliss, D. B. 1973 Water-table visualization of flow-induced pressure oscillations in shallow cavities for simulated supersonic flow condition. *Acoust. Soc. America 86th meeting* (Paper Z13).

Henshaw, M. J. de C. 2000 M219 cavity case. In *Verification and Validation Data for Computational Unsteady Aerodynamics*, *Tech. Rep.* RTO-TR-26, AC/323(AVT)TP/19, pp. 453–472.

Ho, C.-M. & Huang, L.-S. 1982 Subharmonics and vortex merging in mixing layers. *J. Fluid Mech.* **119**, 443–473.

Huang, L.-S. & Ho, C.-M. 1990 Small-scale transition in a plane mixing layer. *J. Fluid Mech.* **210**, 475–500.

Huerre, P. & Rossi, M. 1998 Hydrodynamic instabilities in open flows. In *Hydrodynamics and Nonlinear Instabilities* (ed. C. Godrèche & P. Manneville), pp. 81–214. Cambridge University Press.

Karamcheti, K. 1955 Acoustic radiation from two-dimensional rectangular cutouts in aerodynamic surfaces. *NACA TN* 3487.

Kegerise, M. A., Spina, E. F., Garg, S. & Cattafesta III, L. N. 2004 Mode-switching and nonlinear effects in compressible flow over a cavity. *Phys. Fluids* **16**, 678–687.

Kim, Y. C. & Powers, E. J. 1979 Digital bispectral analysis and its application to nonlinear wave interactions. *IEEE Trans. Plasma Sci.* **7**, 120–131.

Knisely, C. & Rockwell, D. 1982 Self-sustained low-frequency components in an impinging shear layer. *J. Fluid Mech.* **116**, 157–186.

Komerath, N. M., Ahuja, K. K. & Chambers, F. W. 1987 Prediction and measurement of flows over cavities – a survey. *AIAA Paper* 87-0166.

Larchevêque, L., Sagaut, P., Mary, I., Labbé, O. & Comte, P. 2003 Large-eddy simulation of a compressible flow past a deep cavity. *Phys. Fluids* **15**, 193–210.

Lenormand, E., Sagaut, P., Ta Phuoc, L. & Comte, P. 2000 Subgrid-scale models for large-eddy simulation of compressible wall bounded flows. *AIAA J.* **38**, 1340–1350.

Lin, J. C. & Rockwell, D. 2001 Organized oscillations of initially turbulent flow past a cavity. *AIAA J.* **39**, 1139–1151.

Mary, I. & Sagaut, P. 2002 LES of a flow around an airfoil near stall. *AIAA J.* **40**, 1139–1145.

Maull, D. J. & East, L. F. 1963 Three-dimensional flow in cavities. *J. Fluid Mech.* **16**, 620–632.

Michalke, A. 1965 On spatially growing disturbances in an inviscid shear layer. *J. Fluid Mech.* **23**, 521–544.

Miksad, R. W. 1972 Experiments on the nonlinear stages of free-shear-layer transition. *J. Fluid Mech.* **56**, 695–719.

Monkewitz, P. A. & Huerre, P. 1982 The influence of the velocity ratio on the spatial instability of mixing layers. *Phys. Fluids* **25**, 1127–1143.

Pechier, M., Guillen, P. & Cayzac, R. 2001 Magnus effect over finned projectiles. *J. Spacecraft Rockets* **38**, 542–549.

Plumbee, H. E., Gibson, J. S. & Lassiter, L. W. 1962 A theoretical and experimental investigation of the acoustic response of cavities in an aerodynamic flow. *Tech. Rep.* WADD-TR-61-75. US Air Force.

Powell, A. 1961 On the edgetone. *J. Acoust. Soc. Am.* **33**, 395–409.

Raverdy, B., Mary, I., Sagaut, P. & Liamis, N. 2003 High-resolution large-eddy simulation of flow around low-pressure turbine blade. *AIAA J.* **41**, 390–397.

Rockwell, D. & Knisely, C. 1979 The organized nature of flow impingement upon a corner. *J. Fluid Mech.* **93**, 413–432.

Rockwell, D. & Knisely, C. 1980 Observations of the three-dimensional nature of unstable flow past a cavity. *Phys. Fluids* **23**, 425–431.

Rockwell, D. & Naudascher, E. 1978 Review – self-sustaining oscillations of flow past cavities. *J. Fluids Engng* **100**, 152–165.

Roshko, A. 1955 Some measurements of flow in a rectangular cutout. *NACA TN* 3488.

Rossiter, J. E. 1964 Wind-tunnel experiments on the flow over rectangular cavities at subsonic and transonic speeds. *Rep. Mem.* 3438. Aeronautical Research Council.

Rowley, C. W., Colonius, T. & Basu, A. J. 2002 On self-sustained oscillations in two-dimensional compressible flow over rectangular cavities. *J. Fluid Mech.* **455**, 315–346.

Sarohia, V. 1975 Experimental and analytical investigation of oscillations in flows over cavities. PhD thesis, California Institute of Technology.

Shieh, C. M. & Morris, P. J. 2001 Comparison of two- and three-dimensional turbulent cavity flows. *AIAA Paper* 2001-0511.

Spee, B. M. 1966 Wind tunnel experiments on unsteady cavity flow at high subsonic speeds. In *AGARD Current Papers*, vol. 4, pp. 941–974.

Tam, C. K. W. 1976 The acoustic modes of a two-dimensional rectangular cavity. *J. Sound Vib.* **49**, 353–364.

Tam, C. K. W. & Block, P. J. W. 1978 On the tones and pressure oscillations induced by flow over rectangular cavities. *J. Fluid Mech.* **89**, 373–399.

Tam, C. K. W. & Morris, P. J. 1985 Tone excited jets part V: a theoretical model and comparison with experiment. *J. Sound Vib.* **102**, 119–151.

Vreman, B., Geurts, B. & Kuerten, H. 1995 *A priori* tests of large-eddy simulation of compressible plane mixing layer. *J. Engng Maths* **29**, 299–327.